Accepted for publication in Mechanical Systems and Signal Processing (2026), Article 114786.
Open access (CC BY 4.0). DOI: 10.1016/j.ymssp.2026.114786

Full-Field Full-Stress-Tensor Identification of Base-Excited Structures

Jaša Šonc[a], Klemen Zaletelj[a], Janko Slavič[a,*]

[a] *University of Ljubljana, Faculty of Mechanical Engineering, Aškerčeva 6, 1000 Ljubljana, Slovenia*

Abstract

Identifying the full-stress tensor over the surface of a vibrating structure is essential for design validation and vibration-fatigue-life estimation, yet current experimental methods provide only pointwise or incomplete stress data. Infrared cameras can provide non-contact, full-field surface-stress measurements on vibrating structures via the thermoelastic effect; however, they measure only the first stress invariant (*i.e.*, the sum of the normal stresses at the free surface: $\sigma_{xx} + \sigma_{yy}$). The individual stress components (σ_{xx}, σ_{yy}, τ_{xy}) required for a complete characterization of the surface-stress state remain inaccessible from a single thermoelastic measurement. This article introduces a method that recovers the full-field, in-plane-stress power spectral density (PSD) field from thermoelastic camera data on a base-excited structure, demonstrated for thin, isotropic, metallic, plate-like structures under adiabatic conditions. First, a characterization measurement identifies the hybrid stress-mode shapes containing all the plane-stress components by merging thermoelastic camera data with a simplified FE model through SEMM. Then, during operation under broadband random base excitation, the camera response is projected onto these mode shapes and expanded to the full-stress-tensor PSD. The method is validated experimentally on a clamped aluminium plate, identifying spatially resolved stress PSDs for all three in-plane components (σ_{xx}, σ_{yy}, τ_{xy}). The full-field first invariant $\sigma_{xx} + \sigma_{yy}$ is measured experimentally; the individual components σ_{xx}, σ_{yy} and τ_{xy} are reconstructed through an experimentally corrected modal expansion informed by an FE stress basis, which supplies the inter-component ratios.

*Corresponding author
Email address: `janko.slavic@fs.uni-lj.si` (Janko Slavič)

Keywords: thermoelastic stress analysis, power spectral density, multiaxial vibration fatigue, SEMM, modal expansion, infrared camera

---

Highlights

- Full stress-tensor PSD identified from a single measured thermoelastic invariant.
- Stress components reconstructed by experimentally corrected, FE-informed expansion.
- Cross-spectral information preserved between stress components.
- Experimental validation on a base-excited aluminium plate.
- Stress PSD fields enable spectral fatigue-life estimation.

1. Introduction

Identifying the full-stress tensor over the surface of a vibrating structure is a fundamental requirement in experimental structural dynamics: it supports design validation, structural health monitoring, and damage assessment under operational loading conditions. In vibration fatigue, structures subjected to dynamic excitation exhibit multiaxial stress states [1], where the response at each surface point is characterized by a full-stress PSD matrix containing the auto- and cross-spectral densities of all the stress-tensor components [2, 3]. Access to this matrix enables, for example, a spectral vibration-fatigue-life estimation, where damage is computed directly from the stress PSD, an approach pioneered by Dirlik [4] and Tovo–Benasciutti [5], recently surveyed in [6, 7], and extended to the multiaxial case through criteria based on equivalent-stress PSD [8, 9], stress-invariant combinations [10], or multi-axis damage spectra [11]. These modern spectral multiaxial criteria all require the full stress-tensor PSD as their input [12]. Yet obtaining the full-stress PSD matrix experimentally over the full surface of a vibrating structure remains an open challenge.

Currently, the stress PSD matrix is computed from finite-element (FE) models through modal superposition and stress frequency-response functions, as introduced by Halfpenny [13] and refined through modal approaches by Braccesi et al. [14] and Mršnik et al. [15]. This requires an accurate numerical model (geometry, material properties, boundary conditions, and damping), and yields computed, not measured, stress fields. Alternatively, strain-gauge rosettes provide the in-plane-stress tensor at discrete surface locations; however, their spatial coverage is inherently sparse, their installation adds mass and wiring, and the gauges themselves are subject to degradation under prolonged dynamic loading [16]. Neither approach delivers spatially dense, experimentally measured stress fields over the full surface of a structure.

Non-contact, spatially dense measurement techniques provide surface-wide data without mass loading and have transformed experimental structural dynamics [17, 18]. Digital image correlation (DIC) [19, 20] and other video-based methods such as triangulation [21] and optical-flow analysis [22] measure dense spatial displacement and derive strain by double spatial differentiation [23]. However, differentiation amplifies the measurement noise, and obtaining stress additionally requires a constitutive model. Scanning laser Doppler vibrometry (LDV) offers excellent velocity sensitivity and bandwidth, but measures only one point sequentially, requires repeatable excitation for scanning, and provides no direct stress information [24]. In contrast, the thermoelastic stress analysis (TSA) camera is a non-contact, full-field technique that directly measures surface stress, bypassing differentiation entirely [18, 25]. Under adiabatic conditions, which for metals typically hold above a few hertz [26, 23], the thermoelastic effect relates the surface-temperature changes to the first stress invariant [27], giving TSA a unique advantage. However, the technique provides only a single scalar quantity, and the individual stress-tensor components remain inaccessible from a single thermoelastic measurement. The interpretation of this single invariant under multiaxial conditions has itself been the subject of recent thermoelastic study, addressing biaxial and mean-stress effects on the stress evaluation [28].

TSA has recently been extended to structural-dynamics applications [29]. Molina-Viedma et al. [30] demonstrated thermoelastic stress-field identification at frequencies exceeding 2 kHz, while Zaletelj et al. [23] showed that full-field stress-mode shapes can be recovered from IR-camera data even when the thermoelastic signal lies below the noise floor, using camera-based hybrid EMA techniques [31]. In parallel, camera-based transmissibility measurements under base excitation have been explored using DIC [32]. Thermoelastic measurements have also been used for modal-based, fatigue-damage identification [33], multiaxial frequency-domain vibration-fatigue assessment [34], and full-field crack detection during vibration testing [35, 36]. The technique has also been extended to rotating structures [37]. Meanwhile, advances in microbolometer technology and calibration [38, 39] are making quantitative TSA increasingly accessible outside dedicated laboratory environments. Despite these advances, all the thermoelastic applications in dynamics have been limited to the first stress invariant; the full-stress PSD tensor has not yet been obtained from camera data alone.

Prior attempts to recover individual stress components from thermoelastic data have combined thermoelastic measurements with hybrid analytical or numerical methods. These classical stress-separation approaches are restricted to static or quasi-static loading [40, 41], and they are inapplicable to vibrating structures under broadband random excitation. In the dynamic domain, modal expansion methods like SEREP [42] and SEMM [43, 44] expand limited displacement or acceleration measurements into full-field responses, including stress [45, 46] and strain fields [47, 48]. Bregar et al. [49] applied SEMM to correct the full-field displacement FRFs measured with a visible-light high-speed camera. Recent substructuring research continues to advance these hybrid formulations, from optimal sensor placement for system-equivalent model mixing [50] to frequency-based substructuring of jointed assemblies [51]. While each of these techniques (thermoelastic stress analysis, modal expansion via SEMM, and transmissibility-based operational identification) is well established individually, they have not been combined to recover the full-field surface-stress tensor from camera data on a vibrating structure. Consequently, the full-stress PSD matrix at every surface point of a vibrating structure has remained accessible only from numerical models or from discrete contact sensors.

This article addresses the recovery of the full-field in-plane-stress PSD matrix (containing σ_{xx}, σ_{yy}, τ_{xy} and their cross-spectra) at every surface point of a thin, isotropic, metallic, plate-like base-excited structure, under adiabatic conditions, from an infrared camera that measures only the first stress invariant $\sigma_{xx} + \sigma_{yy}$. The proposed method combines thermoelastic stress analysis with SEMM-based modal expansion and transmissibility-based operational identification. First, a characterization measurement identifies hybrid stress-mode shapes containing all plane-stress components by merging thermoelastic camera data with a simplified FE model through SEMM. Then, during operation under random base excitation, the camera response is projected onto these mode shapes and expanded to the full-stress-tensor PSD.

The article is organized as follows. The theoretical background for the thermoelastic effect, structural dynamics and substructuring is given in Section 2. The proposed two-step method is presented in Section 3. The method is first validated numerically in Section 4, against an exact full-field finite-element ground truth. Section 5 describes the experimental validation on a base-excited aluminium plate. The last section draws the conclusions. Alternatively to the transmissibility method of Section 3, Appendix A presents an expansion approach that operates from camera data alone, without requiring an accelerometer; however, it provides only real-valued PSDs without any phase information and neglects the cross-modal terms.

2. Theoretical background

2.1. Thermoelastic effect

The thermoelastic effect describes the relation between the stress state and the resulting temperature variations that occur in a material subject to mechanical loading [52, 53]. Under adiabatic conditions, local heating occurs in regions subjected to compression, while local cooling occurs in regions subjected to tension. When a solid material is exposed to harmonic excitation, the cyclic tensile-compressive stresses generate a corresponding harmonic temperature response, which is associated with the first stress invariant (*i.e.*, the sum of the normal stresses) [27]. The amplitude of these temperature variations is typically of the order of millikelvin, which can be detected using high-performance infrared detectors and advanced data-processing techniques [25].

The thermoelastic law is valid only under specific conditions in which the process can be regarded as adiabatic. First, the deformation must remain entirely within the elastic range of the material, ensuring that no plastic deformation or irreversible effects occur. Second, the loading must be relatively fast in which case the heat conduction within the material or to its surroundings is negligible [30]. For metallic materials, these conditions are typically satisfied at excitation frequencies of only a few hertz (*e.g.*, around 5 Hz for aluminium) [26], which implies that adiabatic behaviour is usually achieved in most structural-dynamics applications [23].

Under adiabatic conditions and assuming an isotropic material behaviour, the thermoelastic effect can be expressed as [27, 54]

$$\Delta\sigma_{xx} + \Delta\sigma_{yy} + \Delta\sigma_{zz} = -\Delta T \, \frac{\rho \, c_p}{\alpha \, T_0} \tag{1}$$

or equivalently,

$$\Delta T = K_m \, \Delta\sigma_{kk} \tag{2}$$

where $\Delta\sigma_{kk}$ denotes the sum of the changes in the normal stresses: in all three directions $(\Delta\sigma_{xx}, \Delta\sigma_{yy}, \Delta\sigma_{zz})$ for a general three-dimensional stress condition, or $(\Delta\sigma_{xx}, \Delta\sigma_{yy})$ for plane stresses. The first stress invariant can be measured on the surface of materials using thermal sensors such as infrared thermographic cameras. K_m is the thermoelastic constant [55], which can be obtained from literature or determined with an experimental calibration using strain measurements or numerical calculations [56]:

$$K_{\mathrm{m}} = -\frac{\alpha\, T_0}{\rho\, c_{\mathrm{p}}}, \tag{3}$$

where α is the coefficient of thermal expansion, T_0 is the ambient temperature and ρ and c_{p} are the mass density and specific heat capacity at constant pressure, respectively.

2.2. Stress response of MDOF systems

Complex geometries, which cannot be treated analytically, are instead represented through systems of differential equations, incorporating hysteretic damping and N degrees of freedom (MDOF). The equations of motion, typically assembled using the finite-element method, can be expressed in matrix form [57]:

$$\mathbf{M}\,\ddot{\mathbf{x}}(t) + \mathrm{i}\,\mathbf{D}\,\mathbf{x}(t) + \mathbf{K}\,\mathbf{x}(t) = \mathbf{f}(t), \tag{4}$$

where $\mathbf{x}(t)$ and $\ddot{\mathbf{x}}(t)$ denote the displacement and acceleration vectors, while $\mathbf{M}$, $\mathbf{D}$, and $\mathbf{K}$ represent the mass, damping, and stiffness matrices. The term $\mathbf{f}(t)$ corresponds to the external excitation forces. Assuming harmonic excitation and response: $\mathbf{x}(t) = \mathbf{X}e^{\mathrm{i}\omega t}$ and $\mathbf{f}(t) = \mathbf{F}e^{\mathrm{i}\omega t}$, where ω is the angular frequency and $\mathbf{X}$, $\mathbf{F}$ are the complex amplitude vectors of response and excitation, the equation of motion (4) can be expressed in the frequency domain as [58, 59]:

$$\mathbf{X} = \underbrace{\left(-\omega^2\,\mathbf{M} + \mathrm{i}\,\mathbf{D} + \mathbf{K}\right)^{-1}}_{\mathbf{H}(\omega)}\,\mathbf{F}, \tag{5}$$

where $\mathbf{H}(\omega)$ is the receptance matrix. The receptance matrix $\mathbf{H}(\omega)$ provides the system's response in terms of displacements $\mathbf{X}(\omega)$. However, in vibration-fatigue analysis, the stress response $\mathbf{X}^s(\omega)$ is needed [58]. To obtain it, the r-th displacement mode shape $\boldsymbol{\phi}_r$ is first transformed into the corresponding strain-mode shape $\boldsymbol{\phi}_r^{\varepsilon}$ through the application of the differential operator

$\overline{\mathbf{D}}$ [58]:

$$\boldsymbol{\phi}_r^{\varepsilon} = \overline{\mathbf{D}}\, \boldsymbol{\phi}_r, \tag{6}$$

where:

$$\overline{\mathbf{D}} = \frac{1}{2}\left(\nabla + \nabla^{\mathrm{T}}\right) \tag{7}$$

and ∇ denotes the spatial gradient operator. Under the assumption of small displacements, the r-th stress-mode shape is obtained from the corresponding strain-mode shape using the material stiffness tensor $\mathbf{C}$, which relates stress to strain according to Hooke's law and depends on the Young's modulus E and Poisson's ratio ν for isotropic materials:

$$\boldsymbol{\phi}_r^{s} = \mathbf{C}\, \boldsymbol{\phi}_r^{\varepsilon} \tag{8}$$

The stress-mode shape $\boldsymbol{\phi}_r^s$ is thus the stress-domain counterpart of the classical displacement mode shape $\boldsymbol{\phi}_r$: it carries the same modal information, expressed in stress rather than in displacement [58]. Using these relations, the stress response to a given excitation can be calculated [58, 60]:

$$\mathbf{X}^s(\omega) = \mathbf{C}\, \overline{\mathbf{D}}\, \mathbf{X}(\omega) = \mathbf{H}_{sf}(\omega)\mathbf{F}(\omega) \tag{9}$$

$\mathbf{H}_{sf}(\omega)$ is the stress frequency-response function (FRF) that can be obtained as a sum of the FRFs of all N modes:

$$\mathbf{H}_{sf}(\omega) = \sum_{r=1}^{N} {}_r\mathbf{H}_{sf}(\omega) = \sum_{r=1}^{N} \frac{{}_r\mathbf{A}^s}{\omega_r^2 - \omega^2 + \mathrm{i}\eta_r\omega_r^2}, \tag{10}$$

${}_r\mathbf{A}^s$ is defined as the stress modal constants matrix for the r-th mode [61]:

$${}_r\mathbf{A}^s = \begin{bmatrix} \phi^s_{1r}\phi_{1r} & \cdots & \phi^s_{1r}\phi_{jr} & \cdots & \phi^s_{1r}\phi_{N_\mathrm{d}r} \\ \vdots & \ddots & \vdots & \ddots & \vdots \\ \phi^s_{ir}\phi_{1r} & \cdots & \phi^s_{ir}\phi_{jr} & \cdots & \phi^s_{ir}\phi_{N_\mathrm{d}r} \\ \vdots & \ddots & \vdots & \ddots & \vdots \\ \phi^s_{N_\mathrm{s}r}\phi_{1r} & \cdots & \phi^s_{N_\mathrm{s}r}\phi_{jr} & \cdots & \phi^s_{N_\mathrm{s}r}\phi_{N_\mathrm{d}r} \end{bmatrix}_{N_\mathrm{s}\times N_\mathrm{d}} \tag{11}$$

ϕ^s_{ir} and ϕ_{jr} correspond to the components of the r-th stress- and displacement-mode shapes, $\boldsymbol{\phi}_r^s$ and $\boldsymbol{\phi}_r$, respectively. The total number of degrees of freedom associated with the displacement and stress mode shapes are denoted by N_d and N_s. To evaluate how the structure responds to random loading, the power spectral density (PSD) of the stress response, $\mathbf{S}_{ss}(\omega)$, is computed [58, 62] (the influence of PSD estimation parameters on fatigue-life prediction is discussed in [63]):

$$\mathbf{S}_{ss}(\omega) = \mathbf{H}_{sf}(\omega) \cdot \mathbf{S}_{ff}(\omega) \cdot \mathbf{H}_{sf}^{*\mathrm{T}}(\omega), \tag{12}$$

where $\mathbf{S}_{ff}(\omega)$ represents the excitation force PSD and * denotes the complex conjugate. $\mathbf{S}_{ss}(\omega)$ is of dimension 6×6 for a general three-dimensional stress state or 3×3 for plane stress.

In vibration-fatigue analysis the full FEM model yields a large numerical problem [15]; however, as the frequency-domain solution is limited to the frequency range of interest, only a subset of $M \ll N$ modes needs to be retained. The reduced stress FRF is:

$$\widetilde{\mathbf{H}}_{sf}(\omega) = \sum_{r=1}^{M} {}_r\mathbf{H}_{sf}(\omega) \tag{13}$$

If the natural frequencies are well separated, the stress PSD (12) can be approximated as the sum of per-mode contributions [15]:

$$\widetilde{\mathbf{S}}_{ss}(\omega) \approx \sum_{r=1}^{M} {}_r\mathbf{H}_{sf}(\omega) \cdot \mathbf{S}_{ff}(\omega) \cdot {}_r\mathbf{H}_{sf}^{*\mathrm{T}}(\omega) \tag{14}$$

Each mode contributes independently to the stress PSD field: the spatial shape of each contribution is governed by the stress-mode shape, while the frequency content is governed by the modal FRF and excitation.

2.3. System equivalent model mixing

System Equivalent Model Mixing (SEMM) is a method developed for combining numerical and experimental dynamic models of the same component into a single hybrid model, formulated in the frequency domain [43]. SEMM is based on the dynamic substructuring approach using Lagrange multipliers (LM-FBS) [64] and enables the preservation of the physically significant characteristics of each model without requiring the identification of modal parameters.

SEMM firstly defines a parent model, which establishes the set of degrees of freedom. An overlay model is then applied to introduce the experimentally obtained dynamic properties, while a removed model eliminates the numerical properties within the overlapping region. In this way, a hybrid model is obtained with an expanded set of degrees of freedom and an improved representation of the dynamic response. Each model is represented with the admittance matrix $\mathbf{Y}$.

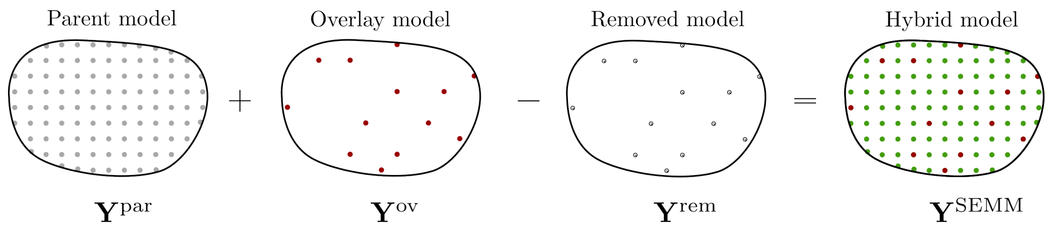

Figure 1: Schematic representation of System Equivalent Model Mixing.

SEMM has already been applied in several contexts, such as the interpolation of spatially sparse experimental data [65] and the merging of measurements from multiple sensors while simultaneously correcting for measurement noise [49]. SEMM has also been modified for use in the modal domain [44].

Within the SEMM, the LM-FBS method [64] is employed to compute a hybrid model by coupling the dynamic properties of two separate models of the same component at their shared degrees of freedom (DOF). The hybrid model is typically constructed by combining a numerical model with an experimental one. The numerical model generally serves as the parent model, providing the complete set of DOFs, while the experimental model acts as the overlay model, introducing the measured dynamic characteristics. The equation of motion for the uncoupled system can then be expressed as follows:

$$\mathbf{u} = \mathbf{Y}(\mathbf{f} + \mathbf{g}), \tag{15}$$

where:

$$\mathbf{Y} = \begin{bmatrix} \mathbf{Y}^{\text{par}} & \mathbf{0} & \mathbf{0} \\ \mathbf{0} & -\mathbf{Y}^{\text{rem}} & \mathbf{0} \\ \mathbf{0} & \mathbf{0} & \mathbf{Y}^{\text{ov}} \end{bmatrix}, \mathbf{f} = \begin{bmatrix} \mathbf{f}^{\text{par}} \\ \mathbf{f}^{\text{rem}} \\ \mathbf{f}^{\text{ov}} \end{bmatrix}, \mathbf{g} = \begin{bmatrix} \mathbf{g}^{\text{par}} \\ \mathbf{g}^{\text{rem}} \\ \mathbf{g}^{\text{ov}} \end{bmatrix} \tag{16}$$

Here, $\mathbf{u}$ denotes the displacement vector, $\mathbf{f}$ the vector of external forces, and $\mathbf{g}$ the vector of internal forces. $\mathbf{Y}^{\text{par}}$ denotes the admittance (FRF) matrix of the parent model (numerical model), $\mathbf{Y}^{\text{rem}}$ corresponds to the removed model, and $\mathbf{Y}^{\text{ov}}$ to the overlay model (experimental model). It should be noted that the admittance of the removed model is taken as negative in order to decouple its dynamics from those of the parent model.

To couple or decouple the different models using the LM-FBS method [64], two conditions must be satisfied at the interface. The first is the compatibility condition:

$$\mathbf{u}_g^{\mathrm{par}} - \mathbf{u}_g^{\mathrm{rem}} = \mathbf{0}; \quad \mathbf{u}_i^{\mathrm{rem}} - \mathbf{u}_i^{\mathrm{ov}} = \mathbf{0}, \tag{17}$$

Three sets of DOFs are distinguished: boundary DOFs (subscript b), located at the interface between the parent and overlay regions; internal DOFs (subscript i), located within the overlay region; and the global set (subscript g), which combines both. The second condition is the equilibrium of forces:

$$\mathbf{g}_b^{\mathrm{par}} + \mathbf{g}_b^{\mathrm{rem}} = \mathbf{0}; \quad \mathbf{g}_i^{\mathrm{par}} + \mathbf{g}_i^{\mathrm{rem}} + \mathbf{g}_i^{\mathrm{ov}} = \mathbf{0}, \tag{18}$$

Equations (17) and (18) can be solved using the LM-FBS method [64]. Reformulating them in the primal notation results in a single-line expression for the hybrid SEMM model [43]:

$$\mathbf{Y}^{\mathrm{SEMM}} = \mathbf{Y}_{gg} - \mathbf{Y}_{gg}^{\mathrm{par}} \left(\mathbf{Y}_{bg}^{\mathrm{rem}}\right)^{+} \left(\mathbf{Y}_{bb}^{\mathrm{rem}} - \mathbf{Y}_{bb}^{\mathrm{ov}}\right) \left(\mathbf{Y}_{gb}^{\mathrm{rem}}\right)^{+} \mathbf{Y}_{gg}^{\mathrm{par}} \tag{19}$$

3. Full-field full-stress-tensor identification of base-excited structures

The goal of this study is to recover the full in-plane-stress PSD matrix from thermoelastic camera measurements on a base-excited structure. The challenge is that the camera provides only the first stress invariant $\sigma_{kk} = \sigma_{xx} + \sigma_{yy}$ (2), a single scalar per pixel, whereas for the in-plane stress, three independent stress components (σ_{xx}, σ_{yy}, τ_{xy}) are needed. This section presents a two-step method that identifies the operational plane-stress components.

The key observation is that, for a given mode r, the ratios between the stress components within the stress-mode shape $\boldsymbol{\phi}_r^s$ (8) are fixed structural properties, independent of the excitation [59]. If these inter-component ratios can be identified from a dedicated characterization measurement, then during operation the camera data need only provide scalar modal participation factors; the full-stress tensor can be identified if the assumptions of a linear time-invariant system are met.

The two-step approach is schematically presented in Fig. 2. Step 1 will be discussed in detail in Section 3.1 and identifies the hybrid stress-mode shapes that contain all plane-stress components by merging thermoelastic camera data with the simplified FE model through SEMM (Section 2.3). Step 2 (Sec. 3.2) projects the operational thermoelastic response onto the mode shapes from Step 1 and expands the single-component measurement to the full-stress PSD matrix $\mathbf{S}_{ss}(\omega)$ (12).

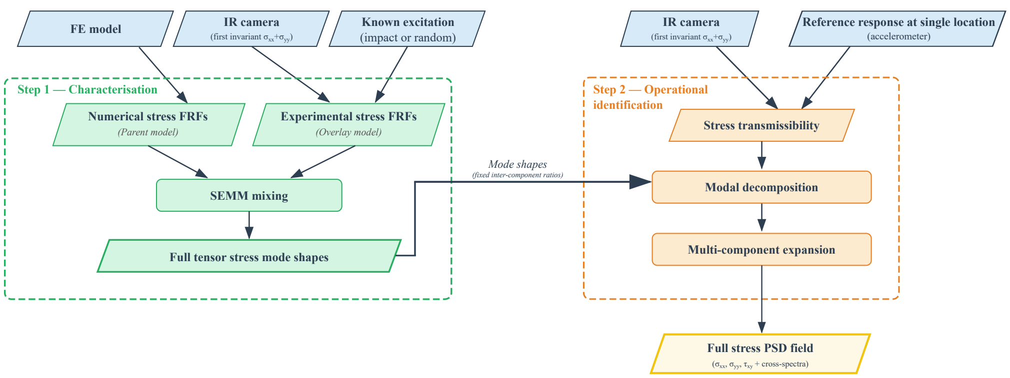

Figure 2: Overview of the proposed two-step method for full-stress-tensor PSD identification, from the measured first-invariant field $\sigma_{xx} + \sigma_{yy}$ to the full stress-PSD matrix including the cross-spectra.

3.1. Step 1: Hybrid stress-mode shapes via SEMM

The goal of Step 1 is to identify the stress-mode shapes that contain all the plane-stress components (σ_{xx}, σ_{yy}, τ_{xy}) while being corrected by the experimentally measured first invariant $\sigma_{xx} + \sigma_{yy}$. This is achieved by applying SEMM (Section 2.3) to thermoelastic stress FRFs (10).

To overdetermine the SEMM coupling and improve its conditioning, excitation is applied at K distinct locations on the stationary structure while the IR camera records the thermoelastic response [23]. Two models are constructed: a numerical parent model from the FE solver, and an experimental overlay model from the IR-camera recordings and the corresponding hammer-impact force signals.

- **Parent model.** A numerically generated finite-element stress FRF matrix (10) $\mathbf{H}_{sf}^{\text{par}}(\omega) \in \mathbb{C}^{4N \times K}$ containing all four stress quantities (σ_{xx}, σ_{yy}, τ_{xy}, $\sigma_{xx} + \sigma_{yy}$) at each of the N FE nodes for every impact case. Here, $4N$ reflects the four stress DOFs per node; the linearly dependent first invariant $\sigma_{xx}+\sigma_{yy}$ is included explicitly as the DOF shared with the camera overlay. The FE model has to be only a rough approximation of the real structure, since SEMM (19) corrects the dynamic response using the experimental overlay.

- **Overlay model.** A camera stress FRF matrix (10) $\mathbf{H}_{sf}^{\mathrm{ov}}(\omega) \in \mathbb{C}^{N_{\mathrm{cam}} \times K}$ containing only the first invariant $\sigma_{xx} + \sigma_{yy}$ at N_{cam} camera pixels for the same K impact cases, obtained via the thermoelastic law (2).

The removed model $\mathbf{H}_{sf}^{\mathrm{rem}}(\omega) \in \mathbb{C}^{N_{\mathrm{cam}} \times K}$ is extracted from the corresponding first-invariant rows of the parent model; these are the numerical DOFs that SEMM (19) replaces with the experimental overlay.

SEMM (19) couples the parent, overlay and removed models at the shared $\sigma_{xx} + \sigma_{yy}$ degrees of freedom: the camera data replace the FE first-invariant response, while the FE model provides the inter-component ratios. The resulting hybrid-stress FRF matrix $\mathbf{H}_{sf}^{\mathrm{SEMM}}(\omega) \in \mathbb{C}^{4N \times K}$ retains all four stress quantities at every FE node, with the first-invariant rows now reflecting the experimentally measured dynamics. Because K independent impact cases are available, the overlay system is (over)determined and the SEMM mixing is well-conditioned.

The stress-mode shapes are identified from $\mathbf{H}_{sf}^{\mathrm{SEMM}}(\omega)$ using the Least-Squares Complex Frequency (LSCF) method [66]. The LSCF estimator fits a common-denominator model to the hybrid stress FRF matrix; the system poles λ_r are selected from a stabilisation diagram, with the identification settings listed in Appendix C and the complete derivation given in the original works [66]. At the stable poles, the hybrid FRF matrix is decomposed into its pole–residue form:

$$\mathbf{H}_{sf}^{\mathrm{SEMM}}(\omega) \approx \sum_{r=1}^{M} \left(\frac{\boldsymbol{\phi}_r^s \, \mathbf{l}_r^{\mathrm{T}}}{\mathrm{i}\,\omega - \lambda_r} + \frac{\boldsymbol{\phi}_r^{s*} \, \mathbf{l}_r^{*\mathrm{T}}}{\mathrm{i}\,\omega - \lambda_r^*} \right), \tag{20}$$

where the residue matrix of each mode factorises into the stress-mode shape $\boldsymbol{\phi}_r^s$ and the participation vector $\mathbf{l}_r$ over the K impact cases. Because Eq. (20) is the pole–residue form of the modal superposition (10), identifying a stress-mode shape from the hybrid SEMM stress FRF is formally identical to identifying a displacement mode shape from a displacement FRF: at each stable pole, the identification returns a stress-mode shape in place of the usual displacement one. The corresponding stress-mode shapes $\boldsymbol{\phi}_r^s$ (8), containing all $4N$ stress DOFs, are extracted at the identified poles. The retained shapes provide the reduced modal basis of the truncated modal sum (14); their modal participation under operational excitation is recovered in Step 2 from the H_1 transmissibility (21).

Each extracted stress-mode shape $\boldsymbol{\phi}_r^s$ contains sub-vectors $\boldsymbol{\phi}_{r,c}^s$ for each stress component $c \in \{\sigma_{xx},\, \sigma_{yy},\, \tau_{xy},\, \sigma_{xx} + \sigma_{yy}\}$. The inter-component ratios are fixed structural properties; they are exploited in Step 2 to expand the camera-measured first invariant to all the stress components.

3.2. Step 2: Transmissibility-based expansion

This subsection defines the central mapping of the proposed method: how the single first-invariant scalar $\sigma_{xx} + \sigma_{yy}$ measured at each camera pixel is expanded into the full 3×3 stress-tensor PSD. Step 1 provides hybrid stress-mode shapes with known inter-component ratios; to recover the full-stress tensor during operation, the modal participation factors at each frequency must be identified. The mapping proceeds in four sub-steps: the first-invariant transmissibility is estimated (Step 2a) and projected onto the Step-1 mode shapes to obtain the modal participation factors (Step 2b), which are then applied through the fixed inter-component ratios of those mode shapes to expand the response to all three plane-stress components (Step 2c) and, finally, to the full stress PSD matrix (Step 2d). During base excitation, the IR camera records the first-invariant stress signal $\sigma_{kk}(t,\, x) = \sigma_{xx}(t,\, x) + \sigma_{yy}(t,\, x)$ at each pixel x via the thermoelastic effect, while an accelerometer on the base provides a reference acceleration $a(t)$. A transmissibility formulation based on the cross- and auto-spectral densities of these two signals extracts the participation factors.

Step 2a — First-invariant stress transmissibility ($\sigma_{xx}+\sigma_{yy}$). The structure is excited by broadband random base excitation and the stress transmissibility at each camera pixel x is estimated with the H_1 estimator [62, 67]:

$$T(\omega,\, x) = \frac{G_{\sigma a}(\omega,\, x)}{G_{aa}(\omega)} \tag{21}$$

where $G_{\sigma a}(\omega,\, x)$ is the cross-spectral density between the camera stress signal and the base acceleration, and $G_{aa}(\omega)$ is the auto-spectral density of the base acceleration. Both spectra are computed via Welch's method. The H_1 formulation removes noise on the camera signal that is uncorrelated with the excitation, making the transmissibility T a consistent estimate of the structural transfer function with units Pa/(m/s^2). The camera provides the transmissibility T for the first invariant $\sigma_{xx}+\sigma_{yy}$ at each pixel; T is a structural property, independent of the excitation level and spectrum.

Step 2b — Modal decomposition. Stacking $T(\omega,\, x)$ over all N_{cam} camera pixels yields the transmissibility vector $\mathbf{T}_{\text{cam}}(\omega) \in \mathbb{C}^{N_{\text{cam}}}$. This vector is projected onto the Step-1 mode shapes using the Moore–Penrose pseudoinverse:

$$\boldsymbol{\gamma}(\omega) = \boldsymbol{\Psi}_{\text{cam}}^{+}\, \mathbf{T}_{\text{cam}}(\omega) \tag{22}$$

where $^+$ denotes the pseudoinverse and $\boldsymbol{\Psi}_{\text{cam}} \in \mathbb{C}^{N_{\text{cam}}\times M}$ collects the Step-1 first-invariant stress-mode shapes ($\sigma_{xx}+\sigma_{yy}$ sub-vectors of $\boldsymbol{\phi}_r^s$) at the camera pixels, with columns $\boldsymbol{\phi}^s_{r,\sigma_{kk}}\big|_{\text{cam}}$ for $r = 1,\ldots,M$ modes. Each component $\gamma_r(\omega)$ is a complex, frequency-dependent participation factor for mode r. For the specimen studied here the projection is well conditioned and two modes suffice ($M = 2$); the conditioning, the mode-number selection and the truncation convergence are examined in Appendix B.3.

Step 2c — Multi-component expansion. The same participation factors $\gamma_r(\omega)$ are used to expand the transmissibility to all three plane-stress components. For each stress component $c \in \{\sigma_{xx},\, \sigma_{yy},\, \tau_{xy}\}$ and spatial location x:

$$T_c(\omega,\, x) = \sum_{r=1}^{M} \gamma_r(\omega)\; \phi^s_{r,c}(x) \tag{23}$$

where $\phi^s_{r,c}(x)$ is the r-th stress-mode shape for component c at location x. The participation factors are extracted from the first-invariant data only; the expansion to the individual stress components relies on the inter-component ratios embedded in the Step-1 mode shapes (8).

Step 2d — Stress PSD. Given the expanded transmissibility, the stress PSD for each component is obtained as:

$$S_c(\omega,\, x) = \left|T_c(\omega,\, x)\right|^2\; S_{aa}(\omega) \tag{24}$$

where $S_{aa}(\omega)$ is the base acceleration PSD. Because the transmissibility is complex-valued, cross-spectral terms between the stress components are also recoverable:

$$S_{cd}(\omega,\, x) = T_c(\omega,\, x)\; S_{aa}(\omega)\; T_d^*(\omega,\, x) \tag{25}$$

where $c, d \in \{\sigma_{xx}, \sigma_{yy}, \tau_{xy}\}$. Equations (24) and (25) together yield the full 3×3 stress PSD matrix at every spatial location.

Because T is a structural property, it can be measured once and reused for any excitation level.

Remark.. The transmissibility-based expansion developed above requires a single accelerometer on the base in addition to the camera. An alternative direct PSD expansion that operates from camera data alone is presented in Appendix A. The transmissibility route is nevertheless adopted as the primary method because the H_1 estimator (21) references the clean base-accelerometer signal, which makes the estimate robust to camera noise while preserving the phase and the cross-spectra; the direct PSD expansion serves as the accelerometer-free fallback, with a quantitative comparison of the two routes given in Appendix A.4.

4. Numerical validation and research

4.1. Ground truth and synthetic experiment

Before the experimental validation, the complete identification chain of Section 3 is tested numerically, against a reference in which the full stress tensor is known exactly. A high-fidelity FE model of the specimen studied experimentally in Section 5 serves as the ground truth: an aluminium plate ($E = 69\,\mathrm{GPa}$, $\nu = 0.33$, $150 \times 150 \times 3\,\mathrm{mm}$) carrying an asymmetric 170 g corner block, with two base-active modes at 51.2 and 187.6 Hz. From this truth model a synthetic thermoelastic recording is generated under random base excitation: the time-varying first invariant $\sigma_{xx} + \sigma_{yy}$ that the camera would capture, together with the base-accelerometer signal. The complete method is then run on this recording exactly as on the measured data, with the SEMM hybrid identification against a deliberately simplified flat-plate prior (no block, generic $E = 63\,\mathrm{GPa}$) followed by the transmissibility-based expansion. The method therefore sees only the first invariant, never the individual components.

A full-field FE ground truth is deliberately used in place of a pointwise reference such as a strain-gauge rosette: independent of the simplified prior and of substantially higher fidelity, it provides a per-component reference at every node and every frequency, free of measurement uncertainty. The comparison is thus openly a model-against-model test of the reconstruction mapping.

4.2. Full-tensor recovery

Against this ground truth, the method recovers the full in-plane stress tensor. Each component is judged by the modal assurance criterion (MAC, spatial pattern), a scale factor (the recovered/true amplitude ratio, 1.00 = no bias) and the relative RMS (magnitude); the resulting metrics are collected in Table 1.

Table 1: Per-component recovery against the full-field FE ground truth (band-RMS stress field, 45–250 Hz).

Component	rel-RMS	scale*	MAC
σ_{xx}	11.5%	1.01	0.987
σ_{yy}	3.8%	1.00	0.999
τ_{xy}	11.3%	0.92	0.993
$\sigma_{xx} + \sigma_{yy}$ (measured invariant)	4.8%	1.00	0.998
von Mises (fatigue driver)†	5.0% / 2.4%	0.98	0.998

* recovered/true amplitude ratio (1.00 = no bias).

† rel-RMS over the whole field / over the top-10% stressed nodes.

The normal stresses and the measured invariant are recovered to within a few percent at near-unity MAC, and the truth-vs-recovered fields in Fig. 3 match component by component (Table 1).

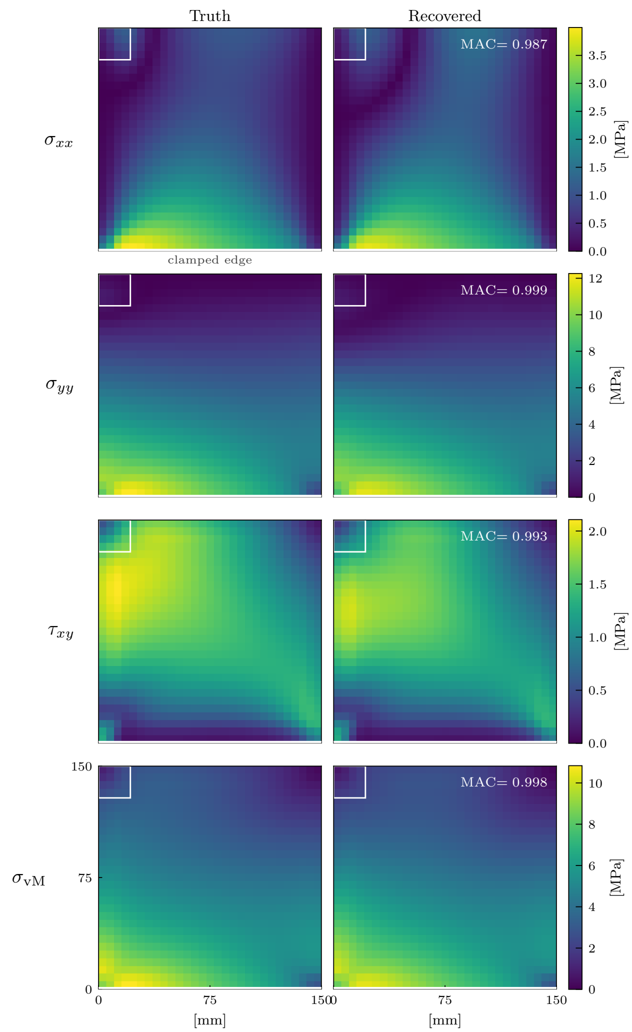

Figure 3: Truth vs. recovered band-RMS (45–250 Hz) fields for σ_{xx}, σ_{yy}, τ_{xy} and the von Mises stress. White outline: corner block.

The shear deserves separate attention, since it is the component the camera cannot observe at all: τ_{xy} is carried entirely by the FE inter-component ratios. It is nonetheless recovered as accurately as σ_{xx} (11.3% against 11.5%), with an essentially exact spatial pattern (MAC 0.993); the per-mode metrics are reported in Table 5, Appendix B.1. The recovery is further detailed in Appendix B.1, where the component-PSD spectra at a representative multiaxial node and the full-field component maps at the first resonance are reported.

The camera-driven SEMM correction carries a quantifiable added value: a pure FE-only prediction errs on the shear by 95%, while the proposed identification recovers it to 11.3%.

4.3. Fatigue and cross-spectral structure

From the recovered full 3×3 stress-PSD matrix, the plane-stress von Mises equivalent-stress PSD is computed as

$$S_{\mathrm{vM}}(\omega) = S_{aa}(\omega) \left[|T_{xx}|^2 + |T_{yy}|^2 - \mathrm{Re}\{T_{xx} T_{yy}^*\} + 3\,|T_{xy}|^2 \right] \tag{26}$$

where T_{xx}, T_{yy} and T_{xy} denote the expanded component transmissibilities of Eq. (23) at the considered location. This is the standard scalar input to spectral vibration-fatigue estimators such as Dirlik or Tovo–Benasciutti [4, 68, 5, 58]. Because all stress components share the same complex modal participation $\gamma_r(\omega)$, the transmissibility route returns the complete complex stress-PSD matrix of Eq. (25); its cross-term $\mathrm{Re}\{T_{xx} T_{yy}^*\}$ enters S_{vM}, which is therefore a genuine full-tensor quantity, obtainable neither from the measured invariant nor from the auto-PSDs alone. In the stress-amplitude domain of Table 1, the recovered von Mises stress matches the exact truth to 5.0% over the field and to 2.4% at the highest-stressed nodes; on the PSD field at resonance, which is quadratic in stress, the same recovery corresponds to 5.8% (Fig. 4). Carried through a Dirlik estimator [4] with a Basquin exponent $b = 5$ and summed over the field, the recovered S_{vM} reproduces the exact fatigue damage to within 6% ($D_{\mathrm{rec}}/D_{\mathrm{tru}} = 0.94$). At an isolated resonance the matrix has rank one (inter-component coherence ≈ 1), a property of any single-input system rather than evidence of multiaxiality; band-integrated over 45–250 Hz, however, approximately 32% of the energy lies outside a proportional state, the multiaxial content required by the spectral fatigue criteria. The dominant σ_{xx}–σ_{yy} cross-term is recovered to approximately 5% in magnitude and to under 1° in phase, the shear cross-terms carry the same accuracy as the τ_{xy} component itself (Section 4.2), and the energy-weighted eigenvalue ratio $\lambda_2/\lambda_1 = 0.007$ over the field (0.001 at the most-stressed nodes) for the truth and the recovery alike: a proportional biaxial core with a small decoupled-shear perturbation, preserved by the recovery. The band-integrated cross-spectral magnitudes and the inter-component coherences are reported in Fig. 17 (Appendix B.1).

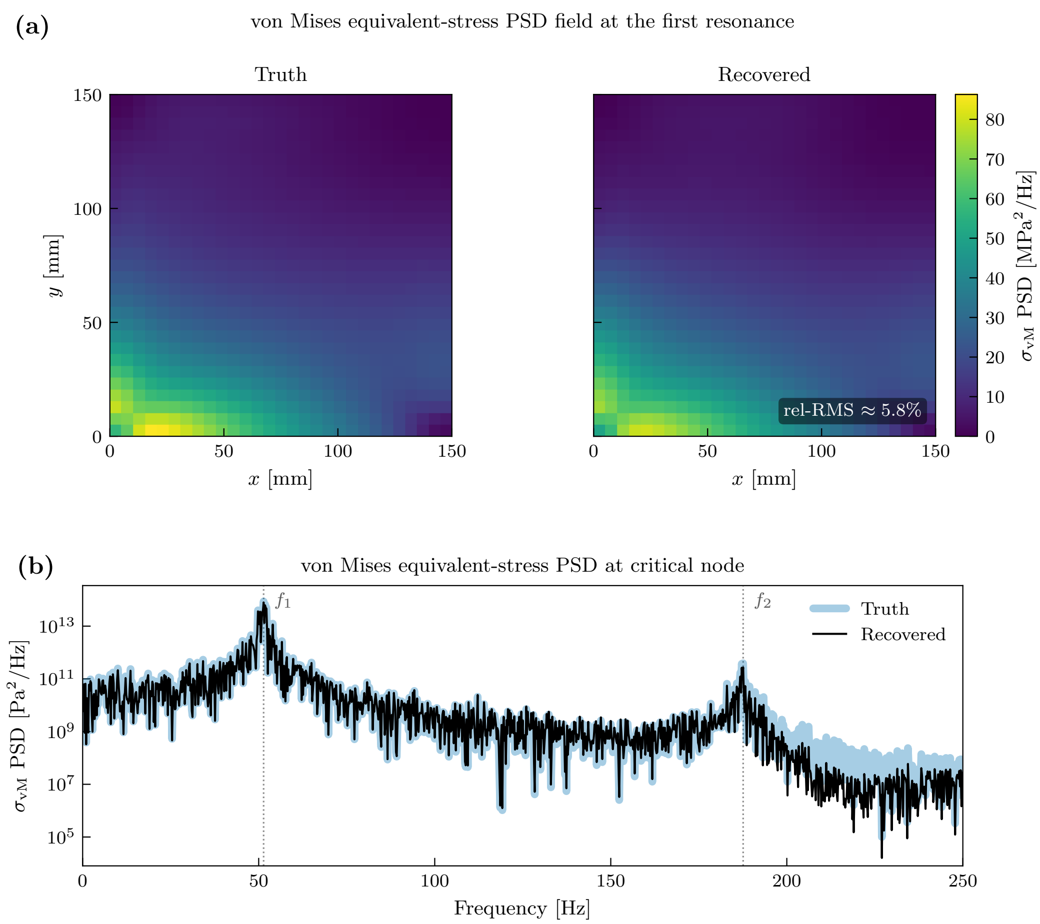

Figure 4: Von Mises equivalent-stress PSD from the recovered 3×3 stress-PSD matrix: (a) PSD field at the first resonance, truth vs. recovered; (b) spectrum at the fatigue-critical node.

5. Experimental validation

The two validations are complementary: the numerical study of Section 4 supplies the exact per-component FE ground truth against which the reconstruction mapping is quantified, while the experimental campaign presented in this section demonstrates the method on a real specimen, a cantilevered aluminium plate excited by random base excitation with two modes within the analysis bandwidth.

5.1. Specimen and instrumentation

The test specimen is an aluminium plate of dimensions $150 \times 150 \times 3$ mm, cantilevered by clamping its bottom edge to a horizontal slip-table adapter with five bolts; the remaining three edges are free. A steel block (170 g) is glued to the back side of the top edge to break the specimen's symmetry and introduce multiaxial stress states. The front surface is coated with high-emissivity, low-reflectivity matt-black spray paint (Wrapper, RAL 9005) to maximise the thermoelastic signal. The paint is applied in several very thin layers to obtain a uniform, near-unity emissivity across the field of view; because every pixel then shares the same radiometric gain, this also removes spatial variation in emissivity as a source of error. The plate is mounted on an IMV A12 electrodynamic shaker with a horizontal slip table (Fig. 5). The thermoelastic response is recorded with a Telops FAST M3k infrared camera at 2000 fps, 132×128 pixel resolution and 200 μs integration time, filming from the front (painted) side. The specimen remains mounted on the shaker throughout both measurement steps.

The numerical model used for SEMM in Step 1 is deliberately kept as a flat clamped plate modelled with shell elements and generic material properties ($E = 63$ GPa, $\nu = 0.33$, $\rho = 2700\,\mathrm{kg/m^3}$) and without the steel block, in order to test the ability of SEMM to correct a roughly approximated model using experimental data.

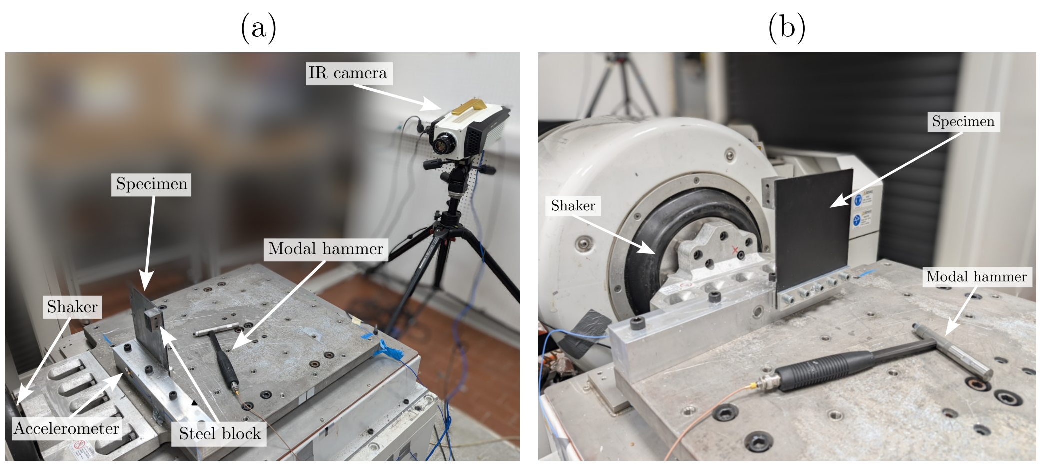

Figure 5: Experimental setup. (a) Overview showing the specimen mounted on the shaker slip table with the IR camera on a tripod. (b) Close-up of the specimen showing the clamped bottom edge and the painted front surface.

5.2. Step 1: Hybrid stress-mode shapes via SEMM

In Step 1, the shaker is turned off and the specimen is excited with a modal hammer at six evenly spaced points on the back side of the plate, leaving the front surface unobstructed for the camera, and providing the multiple independent excitation cases required by SEMM. For this simple plate geometry, convergence was already observed with as few as three impact locations; six were used to improve the signal-to-noise ratio. This convergence is quantified in Fig. 6, which reports the MAC between the stress-mode shape identified from N of the six impacts and the full six-impact reference, evaluated over every choice of the N impact points. Mode 1 (53.7 Hz) is captured from a single impact, while Mode 2 (174.7 Hz) converges by three: its worst single-impact MAC of 0.66 rises to a median of 0.99 at $N = 3$, and the spread over the choice of points collapses accordingly. The identification is thus over-determined and insensitive to the specific impact set. The impact force is measured at each location. The camera records the thermoelastic response; the camera and the force sensor are synchronized via an external trigger signal. The hammer provides broadband excitation; FRFs are analysed over 45–250 Hz, excluding a narrow artifact from the camera's Stirling cryocooler near 40 Hz.

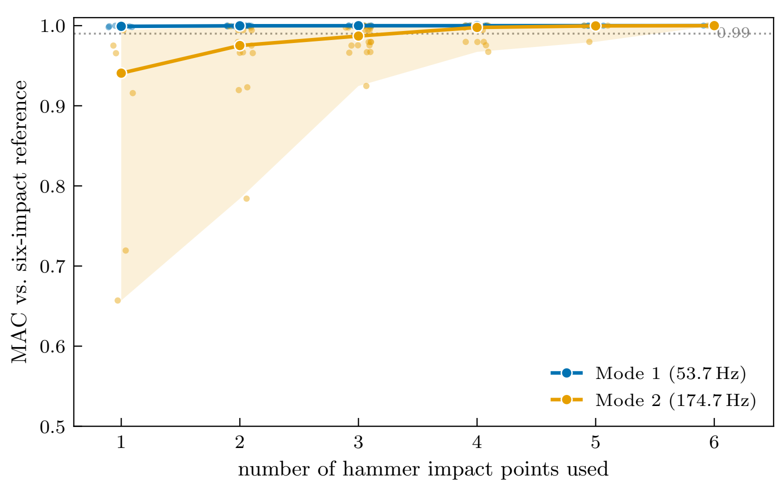

Figure 6: Impact-location robustness of the Step-1 stress-mode shapes: MAC between the mode shape identified from N of the six impacts and the six-impact reference.

Table 2: Step-1 measurement and processing parameters.

Parameter	Value
Camera frame rate	2000 fps
Camera resolution (native)	132×128 pixels
Integration time	$200\,\mu$s
Analysis grid	34×34 ($N = 1156$ nodes)
Analysis bandwidth	45–250 Hz
Spectral estimator	H_1 (Hann window, 50 % overlap)
Impact locations	6
α	$23 \times 10^{-6}\,\mathrm{K}^{-1}$
c_p	$900\,\mathrm{J/(kg\,K)}$
T_0	$\approx 293\,\mathrm{K}$

The IR camera captures the thermal images which are then cropped to the specimen region and downsampled to reduce the measurement noise (Table 2); the downsampled resolution is sufficient for the spatially smooth mode shapes of the tested plate. A Python script generates the FE mesh so that its nodes coincide exactly with the downsampled camera pixel locations, satisfying the shared-DOF requirement of SEMM (Section 2.3). SEMM couples the camera-measured first invariant with the FE model at these shared nodes, as described in Section 3.1. The complete set of implementation and processing parameters for both steps, including the SEMM model construction, the modal identification, the spectral estimation, the synchronisation and the thermoelastic calibration, is collected in Table 7 (Appendix C).

The camera temperature FRFs are computed via the H_1 estimator [62, 67] using the hammer force as a reference and converted to stress units via the thermoelastic law (2) with standard aluminium properties (Table 2). Applying the SEMM-based hybrid identification (19) (Section 3.1) to the hammer-impact measurements yields hybrid-stress FRFs at all N nodes. The stress-mode shapes (8) are extracted using the LSCF method [66] as implemented in the `sdypy-EMA` toolbox [69]. Figure 7 compares the spatial root-mean-square (spatial-RMS), *i.e.*, the RMS computed across all N nodes at each frequency line, of the resulting hybrid FRFs with the camera and FE baselines: the SEMM model tracks the camera response at resonance frequencies while following the FE baseline elsewhere. Figure 8 presents spatial stress maps at two selected resonance frequencies; the FE model alone shows frequency and amplitude deviations from the camera measurement, which SEMM corrects by incorporating the experimental data into the hybrid model.

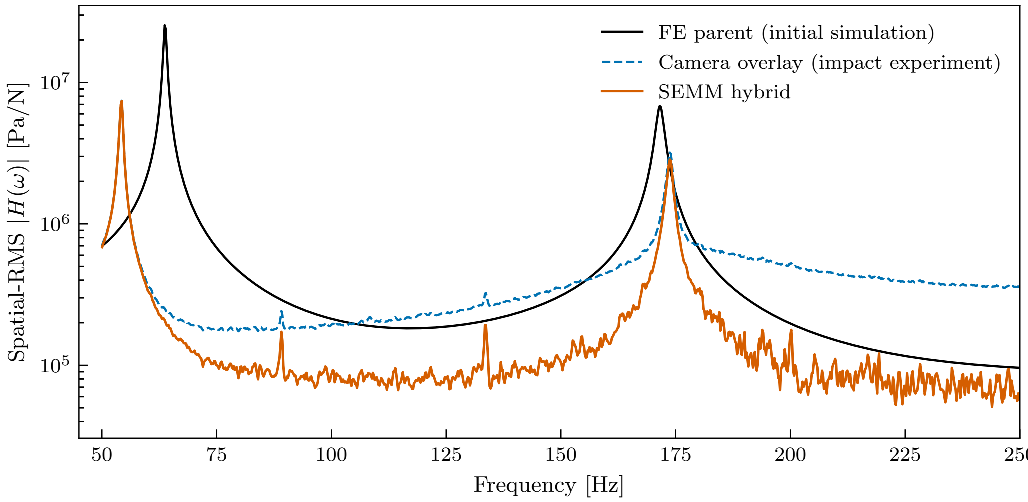

Figure 7: Spatial-RMS of stress FRFs ($\sigma_{xx} + \sigma_{yy}$) for the camera overlay, FE parent, and SEMM hybrid models.

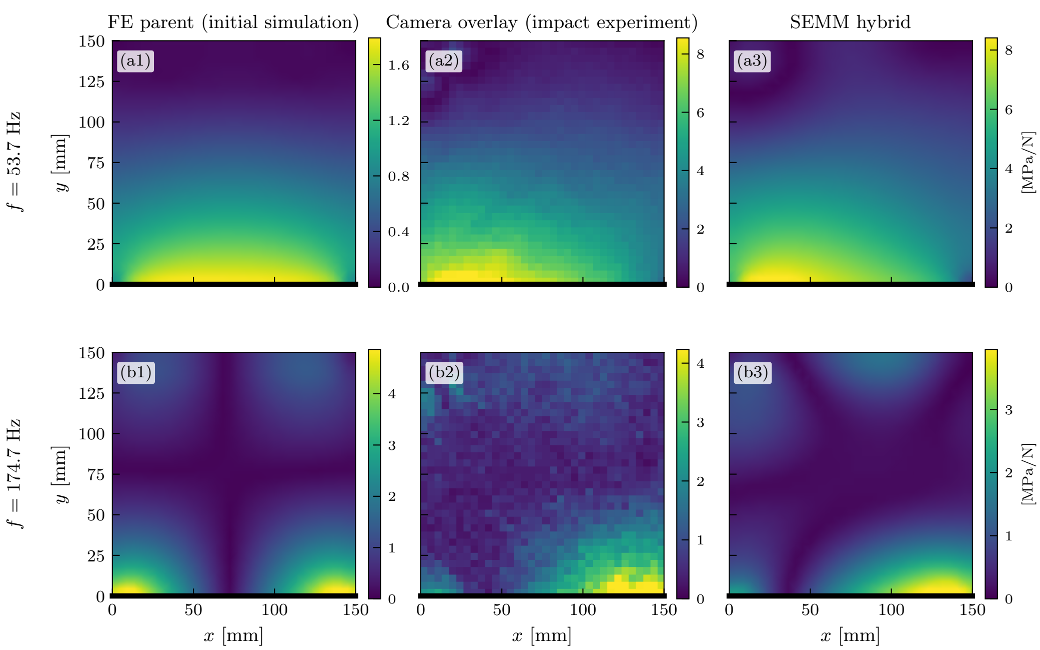

Figure 8: Spatial stress maps ($\sigma_{xx} + \sigma_{yy}$) at the two selected resonance frequencies.

Two modes are identified within the 45–250 Hz analysis band from the hybrid FRFs using the LSCF method (Section 3.1): Mode 1 at 53.7 Hz (first bending) and Mode 2 at 174.7 Hz. Figure 9 displays the extracted stress-mode shapes for all four stress quantities. Mode 1 is dominated by σ_{yy}, consistent with bending about the clamped edge, while τ_{xy} remains small. Mode 2 exhibits a more complex spatial pattern with a notable τ_{xy} contribution, indicative of a combined bending-torsion behaviour. The mode shapes preserve the inter-component amplitude ratios needed for the Step-2 expansion (23).

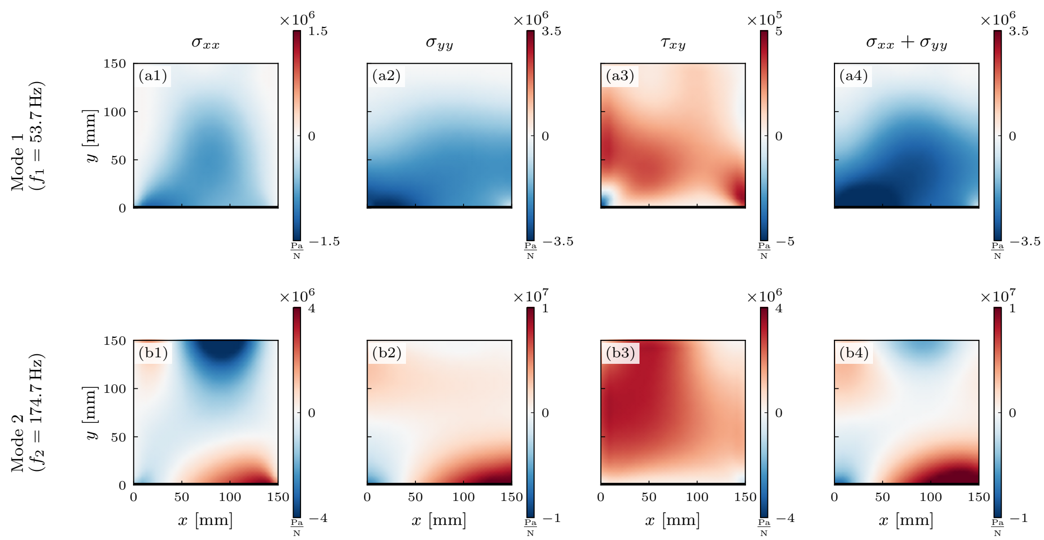

Figure 9: Stress-mode shapes extracted from the SEMM hybrid FRFs for Mode 1 (53.7 Hz, top row) and Mode 2 (174.7 Hz, bottom row). Columns correspond to σ_{xx}, σ_{yy}, τ_{xy}, and $\sigma_{xx} + \sigma_{yy}$.

5.3. Step 2: Transmissibility-based expansion

In Step 2, the shaker delivers a flat random base excitation in the 40–250 Hz band at a PSD level of approximately 0.018 g^2/Hz (RMS $\approx$ 1.9 g). The recording lasts 6 s (12 000 camera frames). The camera records the thermoelastic response, with the camera and a single-axis accelerometer on the base synchronized via an external trigger signal. The accelerometer samples at 25 600 Hz; this is resampled to 2000 Hz via Fourier-based (FFT) resampling to match the camera's frame rate. The transmissibility-based expansion (Section 3.2) is then applied to these synchronized recordings.

Step 2a — First-invariant stress transmissibility ($\sigma_{xx}+\sigma_{yy}$). The stress transmissibility (21) is computed for every camera pixel using the H_1 estimator (Welch's method, Hann window). Under random base excitation, the structure responds strongly only at its resonances. Between the peaks, the thermoelastic signal is weak and the camera noise dominates; the transmissibility is reliable only at the resonance peaks. The full uncertainty and noise-robustness analysis of the identification chain, covering the thermoelastic calibration, the camera noise and the measured coherence, is given in Appendix B.4.

Step 2b — Modal decomposition. The transmissibility field is projected onto the Step-1 mode shapes via the pseudoinverse (22), yielding frequency-dependent modal participation factors $\gamma_r(\omega)$. The magnitudes $|\gamma_r(\omega)|$ peak sharply at the two identified resonances (Fig. 10a), consistent with the Step-1 natural frequencies of 53.7 Hz and 174.7 Hz. As a consistency check, Fig. 10b compares three estimates of the spatial-mean stress PSD for $\sigma_{xx} + \sigma_{yy}$: the raw Welch auto-spectrum, the H_1-denoised PSD, and the PSD reconstructed from only the two retained modes via (24). The progressive reduction from raw to denoised to expanded reflects the removal of the uncorrelated camera noise and the modal truncation; at the resonance peaks, all three curves nearly coincide, confirming that the two retained modes capture the dominant structural response.

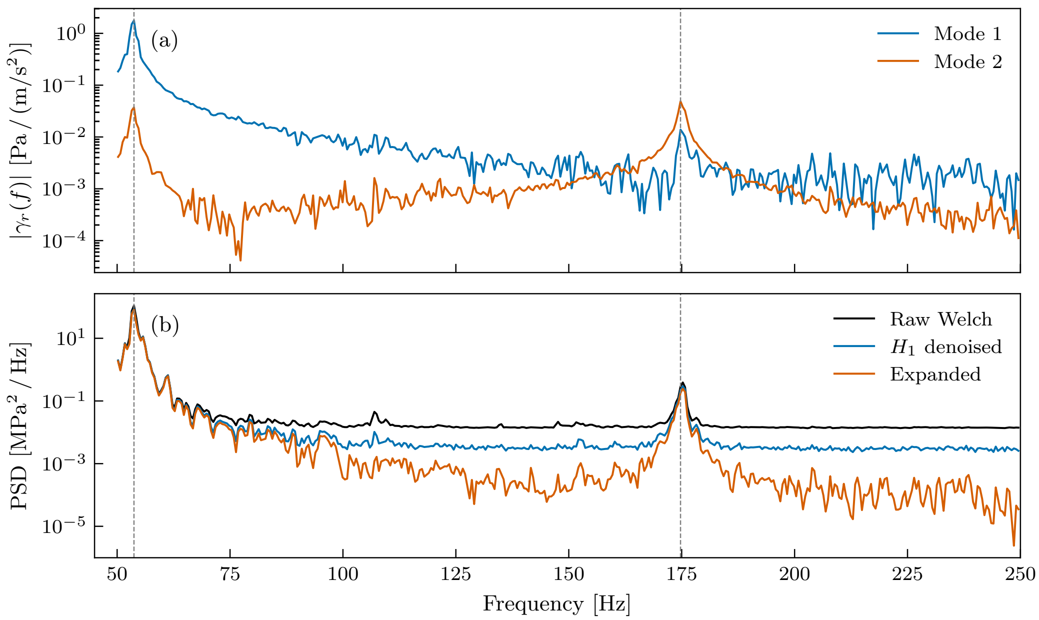

Figure 10: Transmissibility-based expansion overview. (a) Modal participation magnitudes $|\gamma_r(\omega)|$. (b) Spatial-mean stress PSD of $\sigma_{xx} + \sigma_{yy}$: raw camera Welch PSD (black), H_1-denoised PSD (blue), and two-mode expanded PSD (orange).

Step 2c — Multi-component expansion. Using $\gamma_r(\omega)$ and the full-component Step-1 mode shapes, the transmissibility is expanded to all three plane-stress components via (23).

Step 2d — Stress PSD. The stress PSD for each component is obtained via (24). Figure 11 shows the resulting spatial PSD maps at both resonance frequencies. At Mode 1, the response is dominated by σ_{yy} (peak PSD $\approx$ 245 MPa^2/Hz), with σ_{xx} approximately ten times lower and τ_{xy} the smallest. At Mode 2, the overall levels are approximately two orders of magnitude lower, and τ_{xy} exhibits a distinct spatial pattern characteristic of the second mode shape. The spatial-mean PSD spectra across the 40–250 Hz excitation band are shown in Fig. 12.

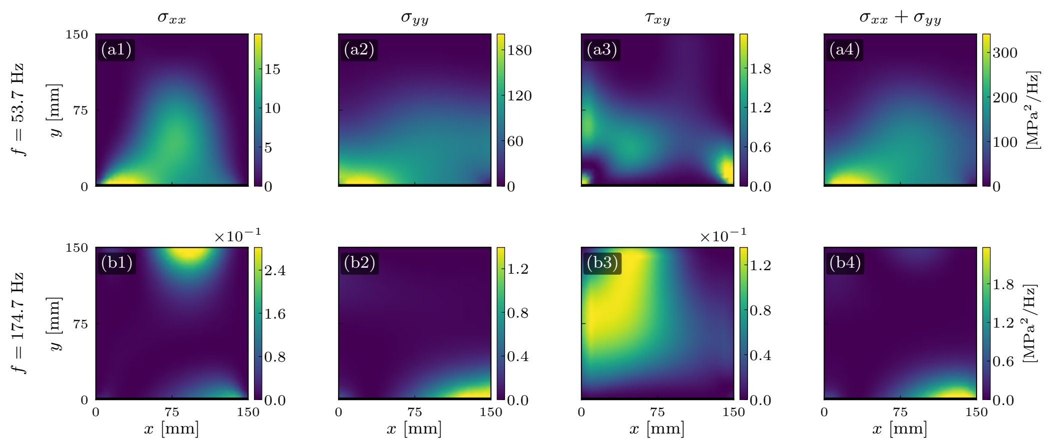

Figure 11: Expanded stress PSD maps at Mode 1 (53.7 Hz, top) and Mode 2 (174.7 Hz, bottom) for all three plane-stress components σ_{xx}, σ_{yy}, τ_{xy} and the first invariant $\sigma_{xx}+\sigma_{yy}$.

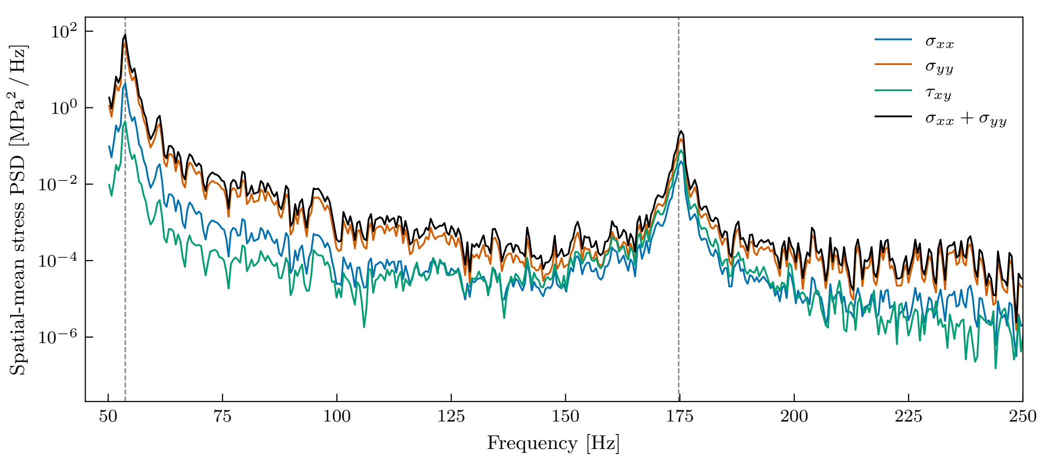

Figure 12: Spatial-mean PSD spectra of the expanded stress components σ_{xx}, σ_{yy} and τ_{xy} across the 40–250 Hz excitation band, showing the recovered individual contributions at both resonance frequencies.

The repeatability of the recovered PSD values is quantified at three critical points: the clamp centre at $(77, 0)$ mm, where the bending stress concentrates, the corner adjacent to the added block at $(23, 127)$ mm, and a mid-field point at $(73, 73)$ mm. Table 3 lists the recovered stress-component PSD at the first resonance, together with a $\pm 1\sigma$ band obtained from a 32-realisation Monte-Carlo study in which an independent camera-noise realisation, at the level calibrated from this recording ($\sigma_T = 10.9\,\mathrm{mK}$ per node), is injected into the measured temperature frames and the full Step-2 identification is repeated. The band is therefore a perturbation-bootstrap estimate of the run-to-run repeatability under camera noise, the dominant stochastic source, the expansion being otherwise deterministic; it remains within 1.3% of the recovered value at every point and component. The underlying noise model is described in Appendix B.4.

Table 3: Recovered stress-component PSD [MPa^2/Hz] at the three critical points at the first resonance (53.7 Hz); the $\pm$ bound is the 1σ Monte-Carlo camera-noise band.

Point (x, y) [mm]	σ_{xx}	σ_{yy}	τ_{xy}
Clamp centre $(77, 0)$	11.357 ± 0.003	110.63 ± 0.03	$(1.436 \pm 0.002) \times 10^{-2}$
Block corner $(23, 127)$	$(5.30 \pm 0.01) \times 10^{-2}$	0.737 ± 0.001	0.0380 ± 0.0003
Mid-field $(73, 73)$	10.589 ± 0.004	53.35 ± 0.01	0.478 ± 0.001

5.4. Discussion

The experimental validation demonstrates the method on a plate geometry; its scope, limitations, and practical aspects are examined below.

The expansion retains only two modes, which capture the dominant structural response of the tested plate, including the multiaxial stress states introduced by the asymmetric tip mass. The natural frequencies identified in Step 1 from the hammer impacts (53.7 Hz and 174.7 Hz) agree with the Step-2 resonance peaks (54.0 Hz and 174.6 Hz) to within less than 1 Hz, confirming consistent boundary conditions and transferable mode shapes. The two-mode truncation is supported by the base-excitation participation argument of Section 3.2, and the numerical convergence study shows the recovery converged from two modes onward, with a truncation error below 2% (Appendix B.3). For structures with denser modal content, several base-active or closely spaced modes, or broadband fatigue analysis covering higher-order modes, a larger retained modal basis is required, which the summed modal expansion (23) accommodates directly.

The reliance on the FE prior for the inter-component ratios is examined by the prior-degradation study of Appendix B.2: the SEMM correction substantially improves the prior whenever the FE error scales or shifts the response, absorbing realistic perturbations of the prior's stiffness, thickness, mass and clamp compliance.

Before arriving at the transmissibility-based approach, a dual-step SEMM expansion, applying SEMM again in Step 2 to directly expand the operational camera response, was also attempted. This approach failed because single-input base excitation produces a rank-1 excitation matrix, insufficient for SEMM, which requires multiple independent input cases (Section 3.1). An alternative expansion route, the direct PSD method, operates without an accelerometer and is presented in Appendix A, together with a comparison of both approaches.

Regarding the experimental procedure, the hammer impacts were applied on the back side of the specimen to leave the camera-facing surface unobstructed; shaker-with-stinger excitation was also tested with equivalent results. Alternatively, impacts could be applied on the camera-facing side by employing advanced image-processing tools to reconstruct the region temporarily obstructed by the hammer.

With regard to scalability beyond the plate geometry studied here, none of the three core steps (the thermoelastic measurement of the first invariant, the SEMM hybrid stress-mode identification and the transmissibility-based modal decomposition) assumes a flat or regular geometry, and the camera-to-FE mapping generalises to non-collocated meshes and curved surfaces. The genuine limitations are the field of view and the surface visibility; mode crowding, which raises the conditioning of the modal projection and, beyond the well-conditioned regime, calls for the truncated-SVD or Tikhonov regularisation discussed in Appendix B.3; and multiple simultaneous base-excitation directions, which require a multi-reference transmissibility formulation with one reference per base degree of freedom. The demands on the camera sampling itself are modest: in the numerical validation, the recovery error stays at the prior-discrepancy floor down to as few as 9 camera points (Appendix B.5). Demonstrations on curved surfaces and with non-collocated camera–FE meshes remain future work.

The stress PSD fields identified by the transmissibility method can serve directly as input to the spectral fatigue methods (such as Dirlik [4], Tovo–Benasciutti [5, 68], and their multiaxial extensions [3] including equivalent-stress [10] and critical-plane criteria [70]), enabling full-surface vibration-fatigue-life estimation without a validated finite-element model (Section 4.3).

Finally, the range of validity of the identification is bounded by the assumptions underlying the thermoelastic signal: plane-stress isotropic linear elasticity, under which the measured temperature variation is proportional to the first stress invariant $\sigma_{xx} + \sigma_{yy}$ (2), and adiabatic conditions, which require the thermal-diffusion length to remain well below the pixel size (satisfied here, but violated in the low-frequency, high-conductivity limit). Anisotropic and composite materials change both the invariant relation and the inter-component split and would require a reformulation of the method; polymers add a mean-stress-dependent response and a low thermal conductivity that narrows the adiabatic window; linearity excludes local plasticity and non-linear boundary conditions; and through-thickness stress gradients in thick structures break the plane-stress assumption. The demonstrated scope of the method is therefore that of thin, isotropic, metallic, plate-like base-excited structures under adiabatic conditions.

6. Conclusions

In this article, the full in-plane stress-tensor PSD (σ_{xx}, σ_{yy}, τ_{xy} and their cross-spectra) of a base-excited structure was identified from a single-invariant thermoelastic camera measurement. The two-step method was validated numerically against an exact full-field FE reference on a multiaxial specimen, and demonstrated experimentally on a clamped aluminium plate with an asymmetric tip mass.

The full-field first invariant $\sigma_{xx} + \sigma_{yy}$ is measured experimentally; the individual components σ_{xx}, σ_{yy} and τ_{xy} are reconstructed through an experimentally corrected modal expansion informed by an FE stress basis, which supplies the inter-component ratios. The SEMM-based Step 1 successfully produces hybrid stress-mode shapes corrected by the camera-measured first invariant. In Step 2, the transmissibility-based expansion achieves effective noise suppression through the H_1 cross-spectral estimator and produces spatially resolved multi-component stress PSD fields with matching resonance frequencies. The cross-spectral terms between the stress components are also recoverable (25). An alternative direct PSD expansion, presented in Appendix A, avoids the need for an accelerometer but produces systematically higher peak amplitudes, attributed to a less effective noise suppression.

Against the exact numerical reference, the measured invariant and the von Mises equivalent stress, the quantity that drives vibration fatigue, are recovered to approximately 5%, and the individual components to approximately 11%, in the stress-amplitude domain. The shear component, which the camera cannot observe, is recovered as accurately as σ_{xx}.

The FE model used in Step 1 was deliberately simplified, with a flat clamped plate without the tip mass and with generic material properties.

SEMM successfully corrected it using the camera data, demonstrating robustness to modelling errors. For the present plate, the convergence of the Step-1 mode shapes was achieved with as few as three hammer impact points (Fig. 6). Six were used to improve the signal-to-noise ratio. Structures with denser modal content would require proportionally more impact locations.

The recovered 3×3 stress-PSD matrix is a direct, full-field input to multiaxial spectral vibration-fatigue methods, and it is obtained without a validated finite-element model, using only a simplified FE prior. The 34×34 spatial grid provides a measurement density comparable to 1156 strain-gauge rosettes distributed over the specimen surface, a measurement density unattainable with contact sensors.

Data availability

The complete processing pipeline and the numerical-validation framework supporting this study are available at `https://github.com/ladisk/papers`, in the directory "Full-field full-stress-tensor identification of base-excited structures".

Acknowledgments

Funding: This work was supported by the Slovenian Research Agency (research core funding No. P2-0263).

References

[1] A. Preumont and Vincent Piefort. Predicting random high-cycle fatigue life with finite elements. *Journal of Vibration and Acoustics*, 116:245–248, 04 1994.

[2] Xavier Pitoiset and André Preumont. Spectral methods for multiaxial random fatigue analysis of metallic structures. *International journal of fatigue*, 22(7):541–550, 2000.

[3] Denis Benasciutti, Frank Sherratt, and Alessandro Cristofori. Recent developments in frequency domain multi-axial fatigue analysis. *International Journal of Fatigue*, 91:397–413, 2016.

[4] Turan Dirlik. *Application of computers in fatigue analysis*. PhD thesis, University of Warwick, 1985.

[5] D. Benasciutti and R. Tovo. Spectral methods for lifetime prediction under wide-band stationary random processes. *International Journal of Fatigue*, 27(8):867–877, 2005.

[6] T. Dirlik and D. Benasciutti. Dirlik and Tovo-Benasciutti spectral methods in vibration fatigue: A review with a historical perspective. *Metals*, 11(9):1333, 2021.

[7] Aleš Zorman, Janko Slavič, and Miha Boltežar. Vibration fatigue by spectral methods—a review with open-source support. *Mechanical Systems and Signal Processing*, 190:110149, May 2023.

[8] Alexander T. Schmidt and Nimish Pandiya. Extension of the static equivalent stress hypotheses to linearly vibrating systems using wave interference – the liwi approach. *International Journal of Fatigue*, 147:106103, 2021.

[9] Xianjun Pei, Sandipp Krishnan Ravi, Pingsha Dong, Xiangwei Li, and Xiaokun Zhou. A multi-axial vibration fatigue evaluation procedure for welded structures in frequency domain. *Mechanical Systems and Signal Processing*, 167:108516, 2022.

[10] Adam Niesłony, Michał Böhm, Robert Owsiński, Artur Dziura, and Karol Czekaj. Integrating von Mises and hydrostatic stresses in frequency domain multiaxial fatigue criteria for vibration fatigue analysis. *Mechanical Systems and Signal Processing*, 224:112229, 2025.

[11] M. Aimé, A. Banvillet, L. Khalij, E. Pagnacco, E. Chatelet, and R. Dufour. A framework proposal for new multiaxial fatigue damage and extreme response spectra in random vibrations frequency analysis. *Mechanical Systems and Signal Processing*, 213:111338, 2024.

[12] E. Proner and E. Mucchi. A multi-axial fatigue damage spectrum for the evaluation of the fatigue damage potential of multi-axis random vibration environments. *Mechanical Systems and Signal Processing*, 226:112362, 2025.

[13] Angela Halfpenny. A frequency domain approach for fatigue life estimation from finite element analysis. *Key Engineering Materials*, 167–168:401–410, 1999.

[14] Claudio Braccesi, Filippo Cianetti, and Lorenzo Tomassini. An innovative modal approach for frequency domain stress recovery and fatigue damage evaluation. *International Journal of Fatigue*, 91:382–396, 2016. Variable Amplitude Loading.

[15] Matjaž Mršnik, Janko Slavič, and Miha Boltežar. Vibration fatigue using modal decomposition. *Mechanical Systems and Signal Processing*, 98:548–556, 2018.

[16] Martin Česnik, Janko Slavič, and Miha Boltežar. Uninterrupted and accelerated vibrational fatigue testing with simultaneous monitoring of the natural frequency and damping. *Journal of Sound and Vibration*, 331:5370–5382, 11 2012.

[17] Patrick O'Donoughue, François Gautier, Erwan Meteyer, Thomas Durand-Texte, Mathieu Secail-Geraud, Félix Foucart, Olivier Robin, Alain Berry, Manuel Melon, Charles Pézerat, Adrien Pelat, and Pascal Picart. Comparison of three full-field optical measurement techniques applied to vibration analysis. *Scientific Reports*, 13:3261, 2023.

[18] Gianluca Rossi. *Mechanical and Thermal Measurements by Images and Waves*. Springer Nature Switzerland, 2026.

[19] T. J. Beberniss and D. A. Ehrhardt. High-speed 3D digital image correlation vibration measurement: Recent advancements and noted limitations. *Mechanical Systems and Signal Processing*, 86:35–48, 2017.

[20] Jaka Javh, Janko Slavič, and Miha Boltežar. High frequency modal identification on noisy high-speed camera data. *Mechanical Systems and Signal Processing*, 98:344–351, January 2018.

[21] Domen Gorjup, Janko Slavič, and Miha Boltežar. Frequency domain triangulation for full-field 3d operating-deflection-shape identification. *Mechanical Systems and Signal Processing*, 133:106287, November 2019.

[22] Ivan Tomac, Janko Slavič, and Domen Gorjup. Single-pixel optical-flow-based experimental modal analysis. *Mechanical Systems and Signal Processing*, 202:110686, 2023.

[23] Klemen Zaletelj, Janko Slavič, Jaša Šonc, and Miha Boltežar. Strain experimental modal analysis of an euler–bernoulli beam based on the thermoelastic principle. *Mechanical Systems and Signal Processing*, 201:110655, 2023.

[24] S. J. Rothberg, M. S. Allen, P. Castellini, D. Di Maio, J. J. J. Dirckx, D. J. Ewins, B. J. Halkon, P. Muyshondt, N. Paone, T. Ryan, H. Steger, E. P. Tomasini, S. Vanlanduit, and J. F. Vignola. An international review of laser Doppler vibrometry: Making light work of vibration measurement. *Optics and Lasers in Engineering*, 99:11–22, 2017.

[25] JM Dulieu-Barton and P Stanley. Development and applications of thermoelastic stress analysis. *The Journal of Strain Analysis for Engineering Design*, 33(2):93–104, 1998.

[26] Charles E. Bakis and Kenneth L. Reifsnider. The adiabatic thermoelastic effect in laminated fiber composites. *Journal of Composite Materials*, 25:809–830, 7 1991.

[27] G. Pitarresi and E. A. Patterson. A review of the general theory of thermoelastic stress analysis. *The Journal of Strain Analysis for Engineering Design*, 38(5):405–417, 2003.

[28] D. Palumbo and R. De Finis. Thermoelastic stress analysis in the presence of biaxial stresses in titanium: effect of the mean stress on errors in stress evaluation. *Experimental Mechanics*, 63(8):1335–1351, 2023.

[29] T. Phan, J.M. Dulieu-Barton, and P. Temarel. Thermoelastic stress analysis of structures under natural vibrations. *Experimental Mechanics*, 46:463–472, 2006.

[30] Ángel J. Molina-Viedma, Luis Felipe-Sesé, Elías López-Alba, and Francisco A. Díaz. Thermoelastic effect in modal shapes at high frequencies using infrared thermography. *Measurement: Journal of the International Measurement Confederation*, 176, 5 2021.

[31] Yonggang Wang, Felix Simeon Egner, Thijs Willems, Matteo Kirchner, and Wim Desmet. Camera-based experimental modal analysis with impact excitation: Reaching high frequencies thanks to one accelerometer and random sampling in time. *Mechanical Systems and Signal Processing*, 170:108879, 2022.

[32] Ángel J. Molina-Viedma, Luis Felipe-Sesé, Manuel Pastor-Cintas, Elías López-Alba, and Francisco A. Díaz. Evaluation of modal identification under base motion excitation using vision techniques. *Mechanical Systems and Signal Processing*, 179:109405, 2022.

[33] Lorenzo Capponi, Janko Slavič, Gianluca Rossi, and Miha Boltežar. Thermoelasticity-based modal damage identification. *International Journal of Fatigue*, 137:105661, 04 2020.

[34] Jaša Šonc, Klemen Zaletelj, and Janko Slavič. Application of thermoelasticity in the frequency-domain multiaxial vibration-fatigue criterion. *Mechanical Systems and Signal Processing*, 224:112002, 2025.

[35] Martin Česnik and Janko Slavič. Temperature–amplitude spectrum for early full-field vibration-fatigue-crack identification. *International Journal of Mechanical Sciences*, 286:109829, 2025.

[36] C.A. Middleton, M. Weihrauch, W.J.R. Christian, R.J. Greene, and E.A. Patterson. Detection and tracking of cracks based on thermoelastic stress analysis. *Royal Society Open Science*, 7:200823, 2020.

[37] Lorenzo Capponi, Klemen Zaletelj, and Janko Slavič. Thermoelasticity-based stress mode-shape identification in rotating structures. *Mechanical Systems and Signal Processing*, 240:113370, 2025.

[38] I. Jimenez-Fortunato, D. Bull, O. T. Thomsen, and J. M. Dulieu-Barton. Quantitative microbolometer-based thermoelastic stress analysis. *Optics and Lasers in Engineering*, 160:107276, 2023.

[39] I. Jiménez-Fortunato, C. Devivier, and J. M. Dulieu-Barton. Assessment of microbolometer infrared cameras for thermoelastic stress analysis. *Strain*, 61(1):e12493, 2025.

[40] P. Stanley. Beginnings and early development of thermoelastic stress analysis. *Strain*, 44(4):285–297, 2008.

[41] Y. M. Huang, H. H. AbdelMohsen, and R. E. Rowlands. Determination of individual stresses thermoelastically. *Experimental Mechanics*, 30(1):88–94, 1990.

[42] John C. O'Callahan, Peter Avitabile, and Robert Riemer. System equivalent reduction expansion process (SEREP). In *Proceedings of the 7th International Modal Analysis Conference (IMAC VII)*, pages 29–37, Las Vegas, NV, USA, 1989.

[43] Steven W.B. Klaassen, Maarten V. van der Seijs, and Dennis de Klerk. System equivalent model mixing. *Mechanical Systems and Signal Processing*, 105:90–112, 2018.

[44] Miha Pogačar, Domen Ocepek, Francesco Trainotti, Gregor Čepon, and Miha Boltežar. System equivalent model mixing: A modal domain formulation. *Mechanical Systems and Signal Processing*, 177:109239, 2022.

[45] Pawan Pingle and Peter Avitabile. Full field dynamic stress/strain from limited sets of measured data. In *Linking Models and Experiments, Volume 2, Conference Proceedings of the Society for Experimental Mechanics Series*, pages 187–200. Springer, 2011.

[46] Marius Tarpø, Bruna Nabuco, Christos Georgakis, and Rune Brincker. Expansion of experimental mode shape from operational modal analysis and virtual sensing for fatigue analysis using the modal expansion method. *International Journal of Fatigue*, 130:105280, 2020.

[47] Marius Tarpø, Tobias Friis, Christos T. Georgakis, and Rune Brincker. Full-field strain estimation of subsystems within time-varying and nonlinear systems using modal expansion. *Mechanical Systems and Signal Processing*, 153:107505, 2021.

[48] M. Pogačar, G. Čepon, and M. Boltežar. Expansion techniques in the modal domain: Practical implementation of M-SEMM and comparative study with SEREP. In *Dynamic Substructures, Volume 4, Conference Proceedings of the Society for Experimental Mechanics Series*. Springer, 2025.

[49] Tomaž Bregar, Klemen Zaletelj, Gregor Čepon, Janko Slavič, and Miha Boltežar. Full-field frf estimation from noisy high-speed-camera data us-

ing a dynamic substructuring approach. *Mechanical Systems and Signal Processing*, 150, 09 2020.

[50] J. M. Nam, S. Y. Park, J. Y. Kim, and Y. J. Kang. Optimal sensor placement method for system equivalent model mixing using correction forces. *Mechanical Systems and Signal Processing*, 237:113150, 2025.

[51] M. Brøns, F. Trainotti, and D. J. Rixen. A novel optimization framework using frequency-based substructuring for estimation of linear bolted joint stiffness and damping. *Mechanical Systems and Signal Processing*, 223:111806, 2025.

[52] W. Thompson. On the dynamical theory of heat. *Earth and Environmental Science Transactions of The Royal Society of Edinburgh*, 20(2):261–288, 1853.

[53] M. A. Biot. Thermoelasticity and Irreversible Thermodynamics. *Journal of Applied Physics*, 27(3):240–253, 1956.

[54] W. Nowacki. *Thermoelasticity, 2nd edition*. Pergamon, Oxford, 1986.

[55] W. N. Sharpe. *Springer Handbook of Experimental Solid Mechanics*. Springer Science and Business Media, 2008.

[56] JM Dulieu-Smith. Alternative calibration techniques for quantitative thermoelastic stress analysis. *Strain*, 31(1):9–16, 1995.

[57] N. M. M. Maia and J. M. M. Silva. *Theoretical and Experimental Modal Analysis*. Research Studies Press, 1997.

[58] Janko Slavič, Matjaž Mršnik, Martin Česnik, Jaka Javh, and Miha Boltežar. *Vibration Fatigue by Spectral Methods*. Elsevier, 2021.

[59] D.J. Ewins. *Modal Testing: Theory, Practice and Application*. Mechanical Engineering Research Studies: Engineering Dynamics Series. Wiley, 2009.

[60] D.B. Li, H.C. Zhuge, and B. Wang. The principle and techniques of experimental strain modal analysis. *Proc of 7th IMAC*, pages 1285–1289, 01 1989.

[61] Tadej Kranjc, Janko Slavič, and Miha Boltežar. A comparison of the strain and the classic experimental modal analysis. *Journal of Vibration and Control*, 7, 12 2014.

[62] K. Shin and J.K. Hammond. *Fundamentals of Signal Processing for Sound and Vibration Engineers*. John Wiley & Sons, 2008.

[63] Kal'avský, Adam and Niesłony, Adam and Huňady, Róbert. Influence of psd estimation parameters on fatigue life prediction in spectral method. *Materials*, 16(3):1007, 2023.

[64] D. de Klerk, D. J. Rixen, and J. de Jong. The frequency based substructuring (fbs) method reformulated according to the dual domain decomposition method. In *Proceedings of the 24th International Modal Analysis Conference (IMAC)*, St. Louis, Missouri, USA, 2006. Society for Experimental Mechanics.

[65] Miha Kodrič, Tomaž Bregar, Gregor Čepon, and Miha Boltežar. An expansion based on system equivalent model mixing: From a limited number of points to a full-field dynamic response. *Measurement*, 190:110522, 2022.

[66] Bart Peeters, Herman Van der Auweraer, Patrick Guillaume, and Jan Leuridan. The PolyMAX frequency-domain method: a new standard for modal parameter estimation? *Shock and Vibration*, 11(3–4):395–409, 2004.

[67] Julius S Bendat and Allan G Piersol. *Random data: analysis and measurement procedures*. John Wiley & Sons, 2011.

[68] R. Tovo. Cycle distribution and fatigue damage under broad-band random loading. *International Journal of Fatigue*, 24(11):1137–1147, 2002.

[69] Janko Slavič, Klemen Zaletelj, Domen Gorjup, D. P. Pasca, A. Aloisio, K. A. Kvåle, G. T. Frøseth, W. Weijtjens, A. Mujtaba, Martin Česnik, Aleš Zorman, G. Tsialiamanis, Ivan Tomac, T. G. Ritto, Domen Ocepek, D. Rohe, O. M. Silva, T. C. P. Masmeijer, K. Čufar, Tomaž Bregar, Miha Kodrič, A. El Mahmoudi, Miha Pogačar, Francesco Trainotti, M. Göldeli, Gregor Čepon, R. Timbó, A. A. Cavallini Jr., V. T. Costa, J. G. F. Santos, A. J. Hughes, J. G. Vargas, A. Fernandes, D. J. Rixen,

K. Worden, and Miha Boltežar. Python open-source signal processing and modeling/simulation for scientific research in structural dynamics – a review. *Mechanical Systems and Signal Processing*, 2025.

[70] Daiyang Gao, Weixing Yao, Weidong Wen, and Jie Huang. A multiaxial fatigue life prediction method for metallic material under combined random vibration loading and mean stress loading in the frequency domain. *International Journal of Fatigue*, 148:106235, 2021.

[71] Charles L. Lawson and Richard J. Hanson. *Solving Least Squares Problems*, volume 15 of *Classics in Applied Mathematics*. SIAM, 1995.

A. Direct PSD expansion

This appendix details the direct PSD expansion introduced in Section 3.2 and compares it with the transmissibility method.

A.1. Non-negative least squares

In structural dynamics, a response PSD can be expressed as a superposition of modal contributions, each weighted by a non-negative modal participation coefficient. Recovering these coefficients from measurements requires solving a linear system in a least-squares sense; however, an unconstrained solution may yield negative weights, which are physically inadmissible for PSD quantities [58]. Non-negative least squares (NNLS) addresses this by explicitly constraining the solution [71]:

$$\min_{\mathbf{x} \geq \mathbf{0}} \|\mathbf{A}\,\mathbf{x} - \mathbf{b}\|^2 \tag{27}$$

where all the elements of $\mathbf{x}$ are required to be non-negative. In the context of PSD decomposition, a measured PSD vector $\mathbf{S}(\omega)$ is expressed as a non-negative linear combination of M basis PSD shapes $\boldsymbol{\psi}_r(\omega)$:

$$\mathbf{S}(\omega) \approx \sum_{r=1}^{M} x_r(\omega)\, \boldsymbol{\psi}_r(\omega) = \mathbf{A}(\omega)\, \mathbf{x}(\omega), \qquad x_r(\omega) \geq 0 \tag{28}$$

where $\mathbf{A}(\omega) = [\boldsymbol{\psi}_1(\omega), \ldots, \boldsymbol{\psi}_M(\omega)]$ collects the basis shapes as columns, $\mathbf{x}(\omega)$ is the vector of non-negative scalar coefficients, and $\mathbf{S}(\omega)$ is the observed PSD at a given frequency ω.

A.2. Method

The method operates entirely on real-valued PSDs and uses the spatial redundancy of the camera pixels for denoising.

Welch auto-spectrum. At each camera pixel x, the Welch auto-spectral density $G_{yy}(\omega, x)$ of the measured first-invariant stress signal $y(t, x)$ is computed. The resulting PSD contains the structural response superimposed with measurement noise.

Virtual-reference denoising. A virtual reference signal is defined as the spatial average of all N_{cam} camera pixels:

$$r(t) = \frac{1}{N_{\mathrm{cam}}} \sum_{i=1}^{N_{\mathrm{cam}}} y_i(t) \tag{29}$$

Because measurement noise at different pixels is uncorrelated, spatial averaging suppresses the noise floor by a factor of $\sqrt{N_{\mathrm{cam}}}$ while preserving the correlated structural response [67]. Using $r(t)$ as reference, a denoised PSD is obtained analogously to the H_1 estimator:

$$S_{\mathrm{clean}}(\omega, x) = \frac{|G_{yr}(\omega, x)|^2}{G_{rr}(\omega)} \tag{30}$$

where $G_{yr}(\omega, x)$ is the cross-spectral density between pixel x and the virtual reference, and $G_{rr}(\omega)$ is the auto-spectral density of the reference. Unlike the transmissibility method (Section 3.2), the camera provides its own reference signal, making an external sensor unnecessary.

PSD decomposition via NNLS. Equation (28) is instantiated with $\boldsymbol{\psi}_r = |\boldsymbol{\phi}^s_{r,\sigma_{kk}}|^2$ and $x_r = \beta_r(\omega)$, giving the denoised camera PSD field as a sum of modal contributions:

$$S_{\mathrm{clean}}(\omega, x) \approx \sum_{r=1}^{M} \beta_r(\omega)\, |\boldsymbol{\phi}^s_{r,\sigma_{kk}}(x)|^2 \tag{31}$$

where $\beta_r(\omega) \geq 0$ are real, non-negative modal participation PSD coefficients determined at each frequency line by NNLS (27).

Multi-component expansion. The expansion to all three plane-stress components follows the same principle as Step 2c of the transmissibility method (Section 3.2), replacing $\gamma_r(\omega)$ with $\beta_r(\omega)$:

$$S_c(\omega, x) = \sum_{r=1}^{M} \beta_r(\omega)\, |\boldsymbol{\phi}^s_{r,c}(x)|^2 \tag{32}$$

Because the method operates on real-valued PSDs, cross-spectral terms between stress components (*e.g.*, between σ_{xx} and σ_{yy}) cannot be recovered. In addition, the resulting stress PSD includes the excitation spectrum and is therefore not directly reusable for different excitation conditions.

A.3. Experimental results

The method of Section A.2 is applied to the same Step-2 camera recording. The noise is suppressed via the virtual reference (29)–(30), and the denoised spectrum lies below the raw Welch PSD (Fig. 13), with the largest reduction away from the resonances.

The denoised PSD field is decomposed onto the squared Step-1 first-invariant mode shapes via NNLS (31), yielding non-negative modal participation coefficients $\beta_r(\omega) \geq 0$ at each frequency line. These coefficients are then used to expand the stress PSD to all three plane-stress components via (32). Figure 13 compares the spatial-mean PSD at three levels: the raw Welch spectrum, the virtual-reference denoised spectrum, and the NNLS-expanded spectrum. The expanded curve closely follows the denoised one at the resonance peaks and removes the remaining off-resonance residuals.

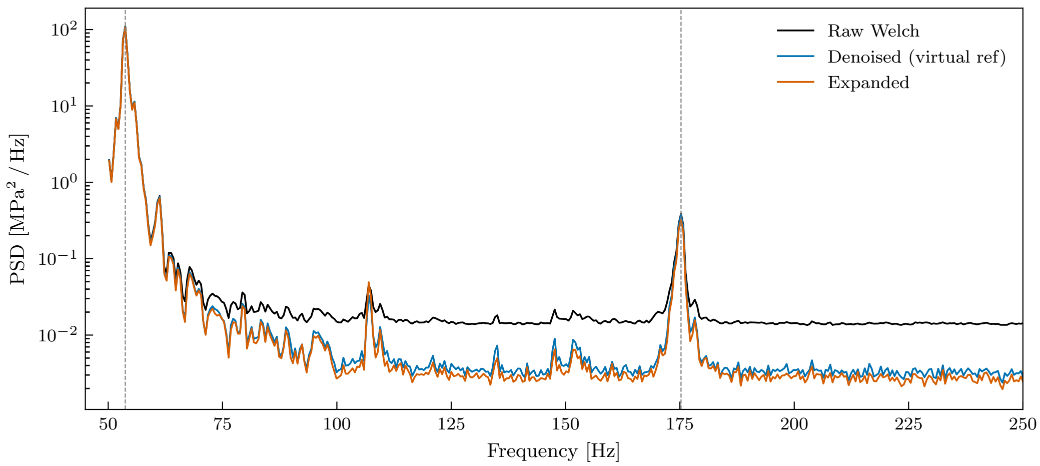

Figure 13: Direct PSD expansion overview. Spatial-mean stress PSD of the first invariant: raw camera Welch PSD (grey), virtual-reference denoised PSD (dashed), and NNLS-expanded PSD (black).

A.4. Comparison with transmissibility method

Both Step-2 methods produce spatially consistent stress PSD fields that share the same resonance frequencies and spatial patterns, confirming that the Step-1 mode shapes are correctly recovered by both expansion routes. Figure 14 compares the spatial PSD maps from the transmissibility-based and direct PSD methods at Mode 1, together with a relative difference map. The spatial distributions are in close agreement; however, the direct PSD method yields peak PSD values approximately 43% higher than the transmissibility method at Mode 1. A similar discrepancy of 42% is observed at Mode 2, indicating a systematic offset rather than a frequency-dependent effect. This difference is attributed primarily to the distinct noise treatment: the H_1 estimator rejects camera noise uncorrelated with the base excitation by construction, whereas the virtual reference (30) relies on spatial averaging, which is less effective, making the transmissibility-based PSD the more accurate estimate at finite record lengths.

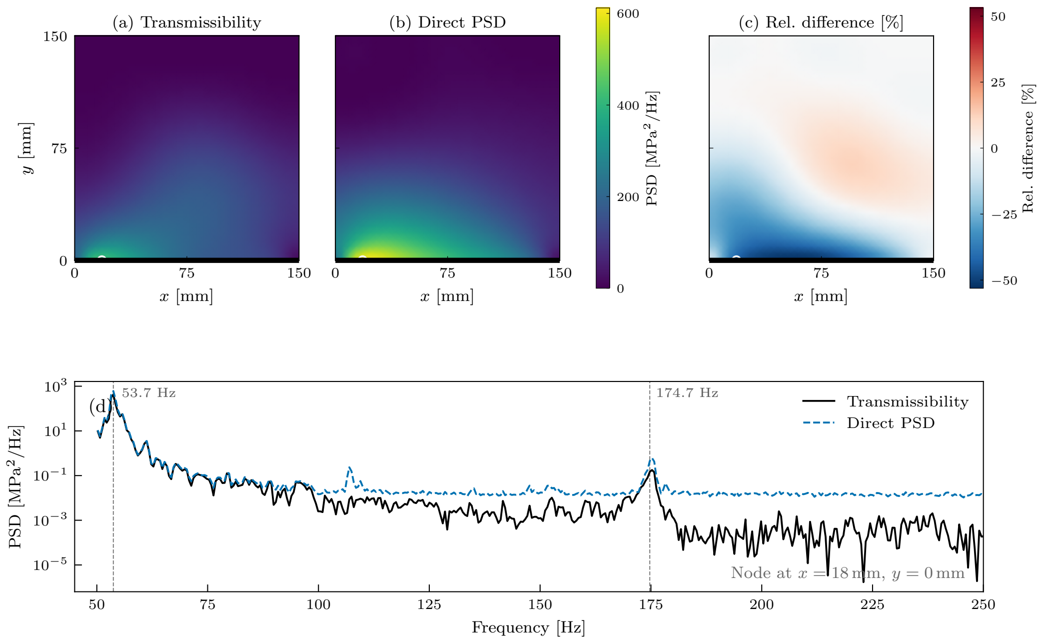

Figure 14: Comparison of the two Step-2 expansion methods. (a) Transmissibility-based stress PSD ($\sigma_{kk} = \sigma_{xx} + \sigma_{yy}$) at Mode 1 (53.7 Hz). (b) Direct PSD expansion at Mode 1. (c) Relative difference between the two. (d) Stress PSD at a representative node ($x = 18$ mm, $y = 0$ mm) for both methods, with resonance peaks marked at 53.7 Hz and 174.7 Hz.

The practical trade-offs between the two methods are summarised in Table 4.

Table 4: Comparison of the two Step-2 expansion methods.

Aspect	Transmissibility (Sec. 3.2)	Direct PSD (Sec. A.2)
Accelerometer	Required (base reference)	Not needed
Denoising mechanism	H_1 estimator	Virtual reference
Modal decomposition	Pseudoinverse on complex transmissibility	NNLS on real PSD
Phase information	Preserved (complex-valued T)	Lost (real-valued PSD)
Reusable across loads	Yes (T is a structural property)	No
Cross-spectral terms	Recoverable	Not recoverable

In the numerical validation of Section 4, both expansion methods are implemented. At zero camera noise both recover the auto-PSDs exactly; under camera noise the H_1 estimator rejects the camera noise uncorrelated with the base signal, so the transmissibility path remains at the prior-discrepancy floor while the accelerometer-free direct-PSD path collapses, its τ_{xy} error rising from 11% to above 130% (Fig. 20, Appendix B.4). In addition, the transmissibility preserves phase and therefore returns the full complex 3×3 stress-PSD matrix required by some multiaxial fatigue criteria; being a structural property, it is also measured once and reused across excitation levels and spectra. The direct-PSD path, by contrast, yields auto-PSDs only.

B. Numerical validation: detailed results, sensitivity and robustness

B.1. Detailed recovery results

Table 5 reports the per-mode recovery of Section 4.2 at the two resonances.

Table 5: Per-mode recovery at the two resonances (stress-amplitude domain).

	Mode 1 (51.2 Hz)		Mode 2 (187.6 Hz)	
Component	amplitude*	MAC	amplitude*	MAC
σ_{xx}	1.01	0.988	1.03	0.962
σ_{yy}	1.00	0.998	0.98	0.995
τ_{xy}	0.91	0.992	0.94	0.996

* recovered/true amplitude ratio (1.00 = exact).

At the representative multiaxial node (Fig. 15), the per-node relative RMS on the PSD is 1.6%, 4.8%, 2.6% and 4.1% for σ_{xx}, σ_{yy}, τ_{xy} and $\sigma_{xx}+\sigma_{yy}$, respectively.

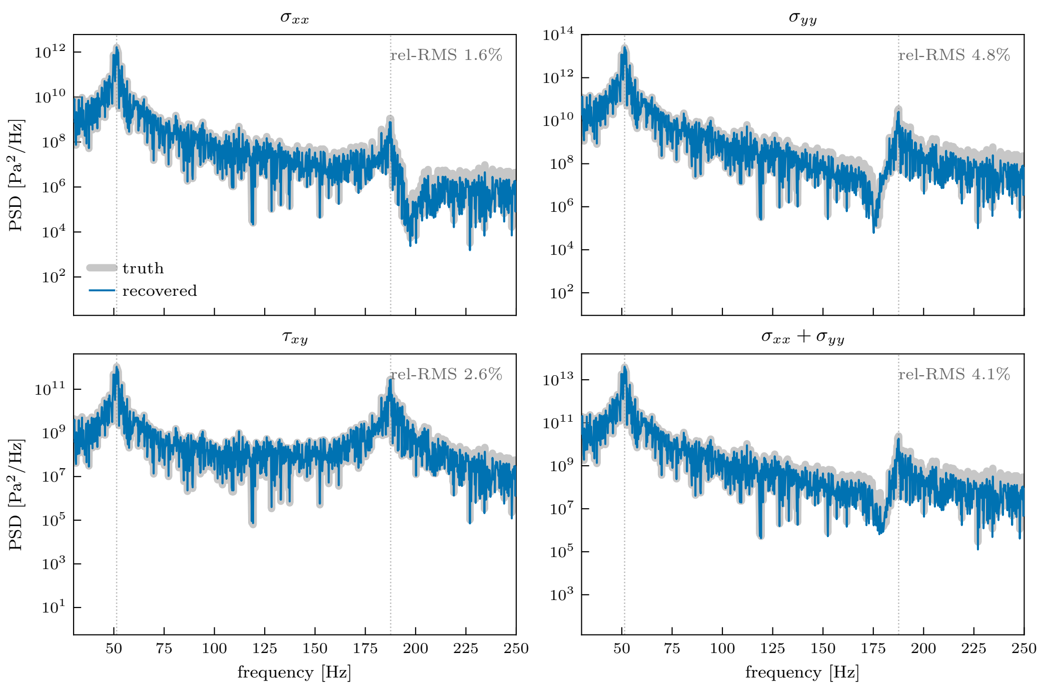

Figure 15: Truth vs. recovered stress-component PSD spectra (σ_{xx}, σ_{yy}, τ_{xy}, $\sigma_{xx} + \sigma_{yy}$) at the representative multiaxial node at (38, 54) mm.

The full-field component maps at the first resonance (Fig. 16) reproduce the truth pattern, the normal-stress PSDs concentrating along the clamped edge and the shear over the interior.

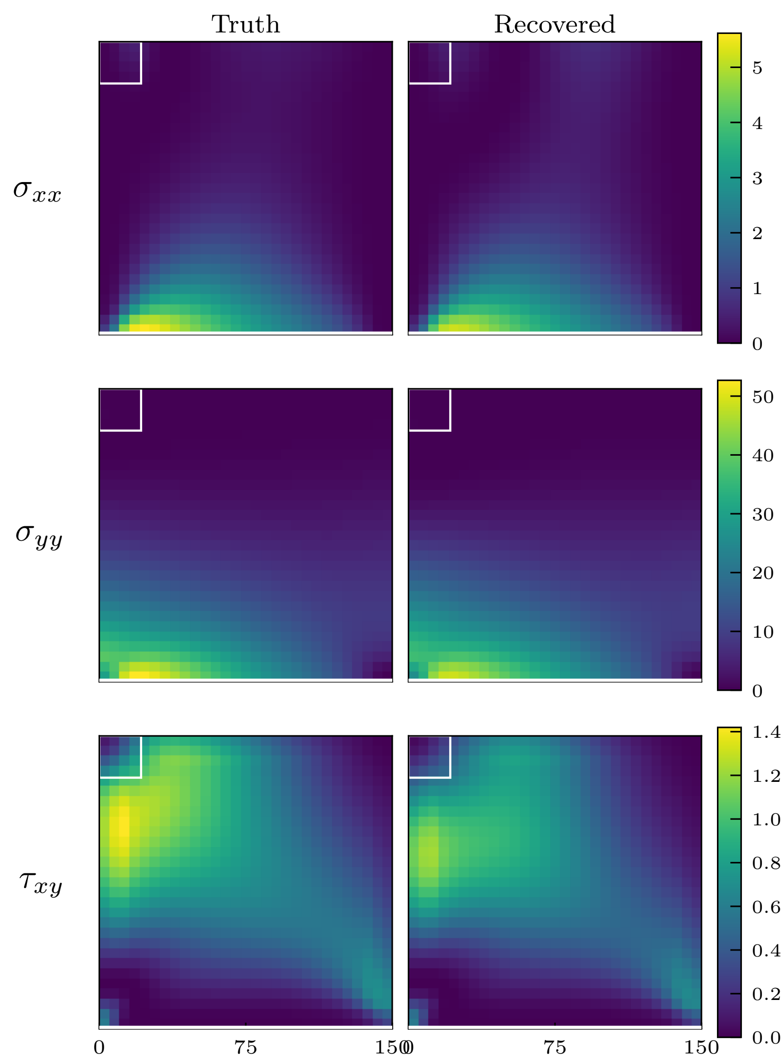

Figure 16: Full-field stress-component PSD maps (σ_{xx}, σ_{yy}, τ_{xy}) at the first resonance, truth vs. recovered. Colour bars in $\mathrm{MPa}^2/\mathrm{Hz}$; white outline: corner block.

The cross-spectral structure of the recovered 3×3 stress-PSD matrix (Section 4.3) is reported in Fig. 17.

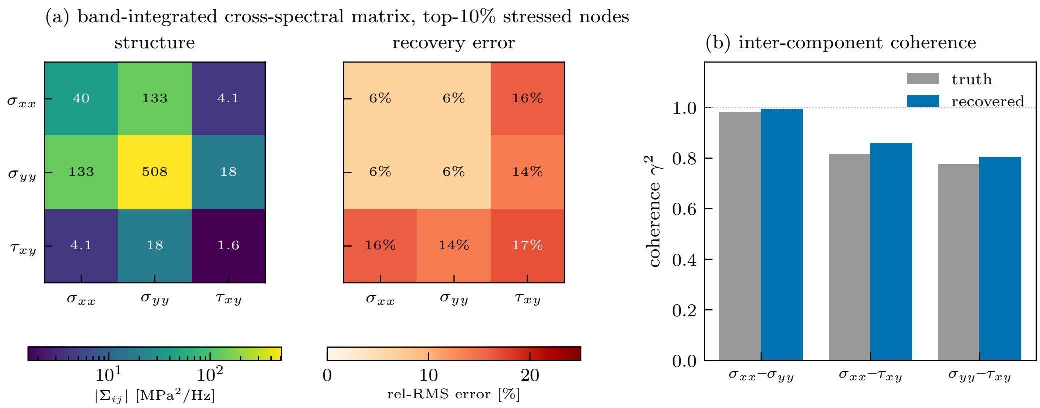

Figure 17: Cross-spectral structure of the recovered 3×3 stress-PSD matrix: (a) band-integrated (45–250 Hz) cross-spectral magnitude $|\Sigma_{ij}|$ at the top-10% stressed nodes, with the per-cell recovery error; (b) inter-component coherence γ^2, truth vs. recovered.

B.2. Sensitivity to the FE prior

In a prior-degradation sweep, individual prior parameters were perturbed and the identification re-run against the same synthetic measurement (Table 6, Fig. 18). Prior errors that only scale or shift the response are absorbed by the SEMM step: Young's modulus is ratio-neutral, cancelling in the transmissibility ratio, and a degradation of the modulus, thickness and density far beyond any realistic modelling error leaves every recovered component essentially unchanged. A realistic clamp compliance is absorbed in the same way, whereas a severe clamp softening, which alters the mode shapes rather than merely rescaling them, degrades the recovery.

Table 6: Sensitivity of the recovered stress components to degradation of the FE prior (band-RMS stress field, 45–250 Hz).

Prior perturbation	Effect on recovered components*
Reference prior ($E = 63$ GPa, flat plate)	σ_{xx} 11.5%, σ_{yy} 3.8%, τ_{xy} 11.3%
Young's modulus 63 $\to$ 69 GPa (ratio-neutral)	0.0%
Young's modulus 63 $\to$ 38 GPa	$\leq$ 0.2%
Thickness 3.0 $\to$ 2.4 mm	$\leq$ 0.2%
Density 2700 $\to$ 2400 kg/m^3	$\leq$ 0.2%
Clamp compliance, realistic (f_1 low by 1.1%)	$\leq$ 0.3%
Clamp compliance, severe (f_1 low by 9.5%)	$\sigma_{xx} \to$ 15.4%, $\tau_{xy} \to$ 18.4%
Poisson's ratio 0.33 $\to$ 0.25	$\sigma_{xx} \to$ 23.0%, $\sigma_{yy} \to$ 6.4%

* "pp" = maximum change in relative-RMS error across the three components, relative to the reference-prior floor.

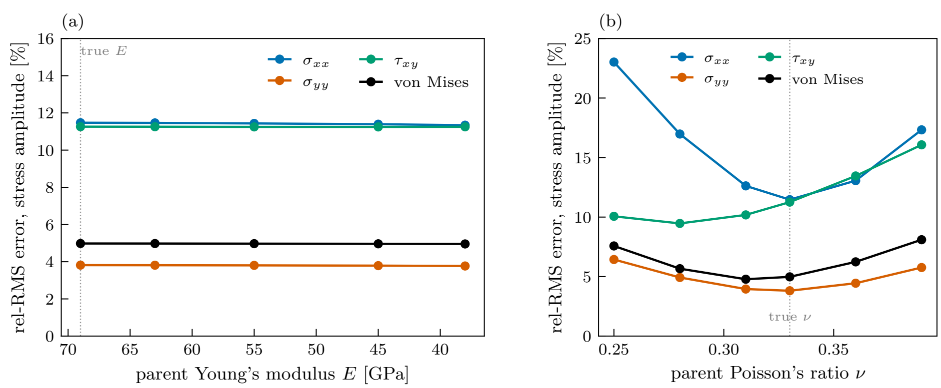

Figure 18: Sensitivity to the FE prior. (a) Error versus the prior's Young's modulus E. (b) Error versus the prior's Poisson's ratio ν.

The one prior parameter that propagates into the recovery is Poisson's ratio, which sets the σ_{xx}:σ_{yy} split left undetermined by the invariant measurement: lowering the prior's ν doubles the σ_{xx} error (Table 6, Fig. 18(b)). A sufficiently accurate ν is therefore required, taken from validated material data or from a separate identification. The component it perturbs is not the fatigue-critical one for the present specimen: at the clamped edge, where the damage concentrates, the von Mises stress is dominated by σ_{yy} (about 80% of the stress at the hotspots), which is both the best-recovered component and essentially flat across the Poisson-ratio sweep. The τ_{xy} residual is set by the prior's omission of the asymmetric block rather than by its stiffness, thickness or mass.

B.3. Modal truncation and projection conditioning

The two-mode truncation was verified by a convergence study: the recovered-stress relative-RMS error is flat from two modes onward (Fig. 19), below 2% over the full excitation band and below 0.2% inside the 45–250 Hz analysis band (which holds over 99.9% of every stress component's response energy), the next structural mode lying at 554 Hz. Under spatially uniform base excitation the antisymmetric modes carry no net participation; of the two retained modes, one dominates the band by energy and the second supplies the multiaxial (shear) content. Built from the full complex modal transmissibilities, the expansion also captures the off-resonant broadband energy between the peaks.

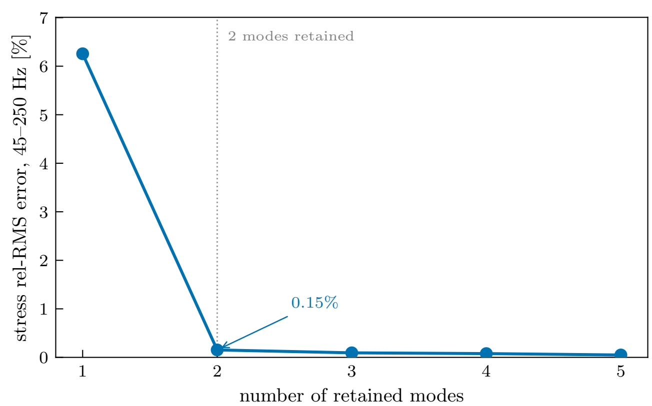

Figure 19: Modal-truncation convergence: recovered-stress relative-RMS error over the 45–250 Hz analysis band versus the number of retained modes, with the true model used as its own prior so that the only error is the truncation.

The corresponding projection is well conditioned: the two first-invariant mode shapes have a normalised inner product of 0.48, and the singular values of $\mathbf{\Psi}_{\text{cam}}$ are 1.21 and 0.72, giving $\kappa(\mathbf{\Psi}_{\text{cam}}) = 1.7$, so no regularisation is applied; dense or strongly correlated modal bases may instead require truncated-SVD or Tikhonov stabilisation.

B.4. Uncertainty and noise robustness

The reconstruction uncertainty comprises a deterministic calibration scaling and a stochastic camera noise. The material parameters α, c_p and T_0 and a uniform surface emissivity enter only through the single scalar gain K_m (3), so an error in any of them rescales every stress amplitude identically; because the stress PSD is quadratic in amplitude, a $\pm x\%$ error in K_m shifts every stress-PSD estimate by approximately $\pm 2x\%$ (a $\pm 10\%$ calibration error giving a uniform $\pm 20\%$ shift) while leaving the spatial patterns, the component ratios and the modal decomposition unchanged. The gain can equally be fixed by a strain gauge co-located with the camera.

Camera thermal noise was assessed by a Monte-Carlo study with the noise level calibrated from the real recordings: spatially uncorrelated Gaussian noise was added to the synthetic first-invariant field and the full identification was repeated over an ensemble of realisations. The recovered field error rises by less than 1% even at $\sigma_T = 100$ mK, about 8× the per-node signal (Fig. 20).

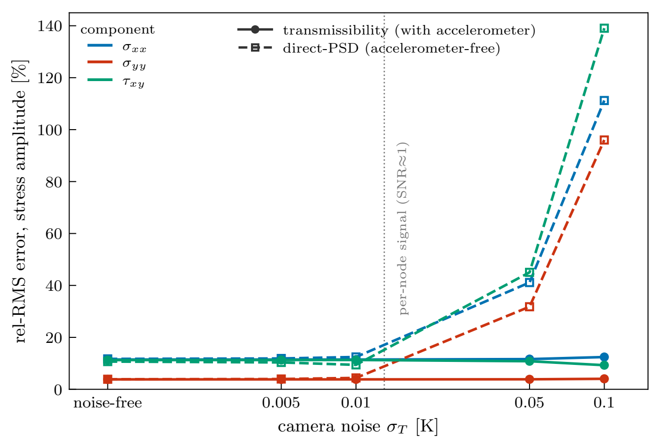

Figure 20: Recovered relative-RMS error (band-RMS stress field, 45–250 Hz) versus the camera-noise level σ_T, for the transmissibility (H_1) path and the accelerometer-free direct-PSD path.

The measured camera–accelerometer coherence over the highest-responding 10% of the field, with Monte-Carlo confidence bands, is $\gamma^2 = 0.78$ at 53.7 Hz and $\gamma^2 = 0.79$ at 174.7 Hz.

B.5. Camera-sampling robustness

Sensitivity to the camera-sampling density was examined by downsampling the synthetic field and re-running the full identification (Fig. 21). Down to as few as 9 camera points the noise-free error stays at the prior-discrepancy floor of about 9%, the two-mode basis being heavily over-determined; with

25% per-point noise the error at 9 points rises from 8.9% to 12%. Partial field of view and limited surface visibility are covered by the same over-determination, provided the retained points span the invariant mode shapes.

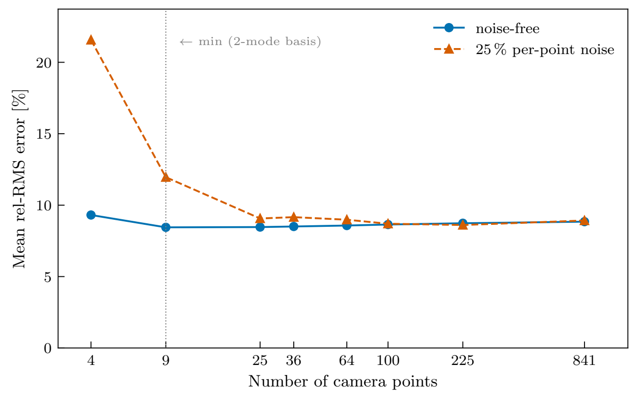

Figure 21: Recovered relative-RMS error (band-RMS stress field, 45–250 Hz, mean over σ_{xx}, σ_{yy} and τ_{xy}) versus the number of retained camera points, noise-free and with 25% per-point noise.

C. Implementation and processing parameters

The parameters that define the two-step identification pipeline are collected in Table 7, grouped by processing stage. The Step-1 measurement parameters common to both steps are listed in Table 2 and are not repeated here. The processing band is wider than the analysis band, so the estimates are formed with margin on either side of the assessed range.

Table 7: Implementation and processing parameters of the full identification pipeline. Parameters shared with Step 1 are listed in Table 2.

Parameter	Value / setting
SEMM hybrid-model construction	
Parent model	simplified flat-plate shell FE; numerical stress FRFs for σ_{xx}, σ_{yy}, τ_{xy} and $\sigma_{xx} + \sigma_{yy}$
Overlay model	experimental first-invariant ($\sigma_{xx} + \sigma_{yy}$) FRFs at the camera interface
Removed model	parent restricted to the camera interface
Coupling	LM-FBS (basic SEMM form)
Stress-mode-shape identification	
Method	LSCF (`sdypy-EMA`)
Model order	selected from the stabilisation diagram (up to order 40)
Pole-acceptance tolerances	1% in frequency, 10% in damping ratio
Retained poles	two base-active modes (53.7, 174.7 Hz)
Mode-shape normalisation	by the norm of the invariant sub-vector
Step-2 acquisition	
Camera recording	12 000 frames (6.0 s at 2000 fps)
Spatial reduction	crop + factor-3 reduction $\rightarrow$ 1156 points (34×34 grid)
Accelerometer sampling	25.6 kHz, resampled to 2000 Hz
Synchronisation	shared external trigger; residual 49-frame (24.5 ms) camera lead removed by cross-correlation
Spectral estimation	
Method	Welch, 5 segments, Hann window
Segment length	3983 samples ($\approx$ 2.0 s)
Frequency resolution	$\Delta f = 0.50$ Hz
Computation band	50–300 Hz (498 lines)
Transmissibility estimator	H_1, $T = G_{\sigma a}/G_{aa}$
Thermoelastic calibration	
Calibration relation	$K_m = -\alpha T_0/(\rho c_p)$
ρ	2700 kg/m^3
$1/K_m$	-3.60×10^8 Pa/K